https://dx.doi.org/10.1016/j.ijheatmasstransfer.2023.124868

Numerical study on the periodic control of supersonic compression corner flow using a nanosecond pulsed plasma actuator

Zongnan Chen(陳宗南)[1], Jiaao Hao(郝佳傲)[1] and Chih-Yung Wen(溫志湧)[1*]

1: Dept. of Aeronautical and Aviation Engineering, The Hong Kong Polytechnic University, Hong Kong, China

* Corresponding author: cywen@polyu.edu.hk

Abstract

This study investigates the effectiveness of a pulsed nanosecond dielectric barrier discharge (NSDBD) plasma actuator for flow control over a supersonic compression corner through numerical simulations. The effects of varying applied voltages, repetitive frequencies, and activated locations of the plasma actuator are examined under large-scale laminar flow separation conditions around a compression corner. The unit Reynolds number and Mach number are 7.8×10^6 m^{-1} and 4, respectively. The results indicate that the discharge induces a pressure rise and leads to misalignment between the pressure gradient and density gradient in the residual heat region. Because of the interaction between the supersonic freestream and the actuation-induced shock/compression flow, convection, compressibility of the fluid element, and baroclinicity of the residual heat region collectively lead to the formation of an induced spanwise vortex, which in turn enables momentum migration. The induced vortex disrupts the initial flow structures and entrains high-energy fluid from the main flow into the boundary layer, promoting momentum mixing between the main flow and the separated flow, which increases the energy of the boundary layer to resist the adverse pressure gradient. The time-averaged flow structures imply that it is possible to totally eliminate the flow separation near the supersonic compression corner. For aerodynamics on the surface, the normal force produces a pitching moment that can be potentially utilized to control the body's orientation

and trajectory. Additionally, total drag on the surface can be reduced by 5%. This suggests that choosing the most appropriate position based on its local fluid characteristics can strongly increase the control effectiveness.

Keywords: *NSDBD; compression corner; flow control; supersonic.*

1. Introduction

As fundamental geometric features, compression corners are widely used in supersonic/hypersonic vehicle components such as wings, engine inlets, and junctions and are generally accompanied by shock wave/boundary layer interactions (SWBLIs). The flow physics of SWBLIs over a compression corner depends on whether the upstream boundary layer state is laminar or turbulent prior to separation. In the case of a laminar interaction, the shock-induced separated flow is highly sensitive to upstream disturbances[1] and can support self-sustained global instabilities[2-4]. Meanwhile, streamwise streaks behind the flow reattachment are commonly observed, which represent the footprints of counterrotating streamwise vortices on the model surface. These streaks can cause significantly elevated peak heating with strong spanwise variations and can promote boundary layer transition downstream of the reattachment. Furthermore, SWBLIs can be unsteady[5, 6]. For a turbulent interaction, the separation shock usually undergoes a back-and-forth motion with a dominant frequency much lower than that of the energetic eddies in the incoming boundary layer, typically by a factor of 0.1 to 0.01. This low-frequency, large-scale unsteadiness can induce an adverse response to the vehicle structure and a degradation in aircraft performance. Similar flow phenomena have been observed in many other canonical configurations. Therefore, it is essential to reduce the size of the separation region and the strength of the separation shock to suppress the generation of counterrotating streamwise vortices, control the low-frequency unsteady motion of the shock system, and consequently reduce the pressure and heat flux peaks.

In recent years, active flow control using plasma actuators has gained significant attention due to its flexibility, high efficiency, and fast response. It has been widely applied to improve aerodynamic performance, including the elimination of flow separation on airfoils[7, 8], drag reduction for various configurations[9, 10], icing mitigation on aircraft[11-13], and the suppression of vortex-induced vibrations in structures[14]. Currently, to effectively control supersonic flow,

three types of plasma actuators have been developed in the literature, namely, plasma synthetic jet actuators (PSJAs)[15], localized arc filament plasma actuators (LAFPAs)[16], and nanosecond surface dielectric barrier discharge (NSDBD) plasma actuators[17]. Among them, NSDBD plasma actuators exhibit unique advantages and potential for active flow control. For example, PSJAs occupy a larger volume, increasing the actuator mass and limiting the spatial arrangement[18]. Moreover, both PSJAs and LAFPAs struggle to maintain uniformity, resulting in strong three-dimensional effects[19]. An NSDBD plasma actuator consists of four main parts: a high-voltage power supply with a nanosecond pulse duration, an exposed electrode, an insulated electrode, and a dielectric barrier between these two electrodes. Following each nanosecond-scale discharge pulse, energy deposition occurs rapidly in the vicinity of the discharge streamers, forming a strong thermalized region. This fast-heating process involves the direct excitation of molecules by electron impacts, followed by rapid quenching or decomposition with "hot" atom formation[20]. Subsequently, an induced shock wave is generated, originating at each discharge streamer and propagating to the surrounding air. Therefore, the residual heat from the energy deposition and the baroclinic vorticity resulting from the interaction between the induced shock wave and the mainstream are the two fundamental characteristics of NSDBD plasma actuators, which are considered the control mechanisms[21, 22]. NSDBD plasma actuators have been used in supersonic flow control as an active flow control method, but there are a limited number of studies. Nishihara et al.[23] attempted to control a Mach 5 flow over a cylinder using an NSDBD plasma actuator, which successfully moved the standing bow shock and increased the shock stand-off distance by up to 25%. Subsequent numerical studies by Bisek et al.[24] and Zheng et al.[21] confirmed the effectiveness of NSDBD plasma actuators in moving the standing bow shock and reducing cylinder drag. Kinefuchi et al. experimentally[25] and numerically[26] investigated the control effects of NSDBD on flow separation induced by an impinging oblique shock over a flat plate, demonstrating the ability of NSDBD plasma actuators to modify boundary layer separation depending on the discharge configuration and pulse repetitive frequency (PRF). They believed that SWBLIs are controlled with NSDBD by two different effects: gas heating by the discharge and vorticity generation due to gas dynamic perturbation, especially in a canted electrode configuration. However, they did not account for changes in vorticity due to the thermal effect itself. While these studies have indicated that NSDBD plasma actuators hold promise for supersonic flow control, there are only a few studies on applying plasma actuators to supersonic compression corners and even fewer using NSDBD plasma actuators. As previously mentioned, the flow physics of supersonic SWBLIs heavily depends on the state of the incoming boundary layer, and the

control effects and mechanisms of NSDBD plasma actuators for both laminar and turbulent interactions remain unclear. Therefore, this paper systematically investigates SWBLI control using NSDBD plasma actuators as a first step. In addition to investigating its effectiveness, this study also focuses on the effects of various parameters, such as the applied voltage, pulse repetitive frequency (PRF), and excitation position, providing an optimized configuration under the given conditions.

The rest of the paper is organized as follows. The geometric configuration and the flow conditions are presented in Section 2. The plasma models and numerical methods are described in Section 3, along with the vortex transport equation and the mesh independence study. Section 4 first presents the induced flow by NSDBD in quiescent air and laminar separation flow over the compression corner studied in this paper. Then, the control effects on the separation bubble region and corresponding aerodynamics are discussed in detail. Finally, the control mechanism is described by analysis of the decomposition of vorticity changes and the instantaneous flow field. Conclusions are provided in Section 5.

2. Geometric configuration and flow conditions

2.1. Ramp model geometry and activation parameters

The compression corner model comprises a flat plate featuring a sharp leading edge, followed by a ramp, with the main details of the compression corner depicted in Fig. 1. The flat plate and ramp have lengths of 60 mm (L_0) and 150 mm (L_r), respectively. For the current numerical investigations, a moderate deflection angle of 10° is selected to ensure a large separation region without the formation of secondary vortices and consequent intrinsic instability[2] under the given freestream conditions. The flow field variables are nondimensionalized by L_0, which is considered the characteristic length of the flow. The characteristic time of the flow t_0 is defined as L_0/U_∞, where U_∞ is the velocity of the freestream.

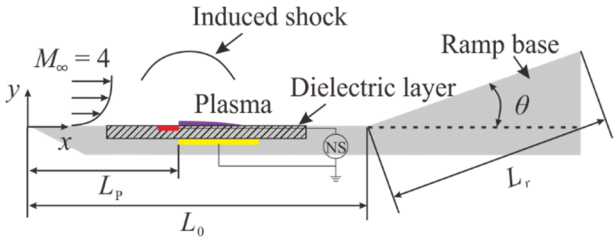

Fig. 1. Schematic of the NSDBD plasma actuator on the compression corner

The NSDBD plasma actuator is placed at different locations above the flat plate, as shown in Fig. 1. The distance L_p is from the leading edge to the starting location of plasma, which usually

occurs at the downstream edge of the exposed electrode. The coordinate system is constructed with the origin located at the leading edge of the flat plate. The *x*-axis is coincident with the flow direction, and the *y*-axis points in the vertical direction. The simulation comprises seven cases that are compared to each other to study the effects of NSDBD at different voltages and streamwise locations. The first case C0 is the basic state without the actuator. The actuation voltages and actuator locations of other cases are listed in Table 1.

Table 1. Simulation cases with different parameters

Case	C0	C1	C2	C3	C4	C5	C6
V (kV)	-	25	25	25	50	50	50
L_p / L_0	-	0.33	0.50	0.67	0.33	0.50	0.67

Furthermore, different PRFs depending on the flow characteristic time are studied to compare the control performance of periodic activation. Equation 1 defines the dimensionless frequency F^+. Three different F^+ values of 1, 10, and 20 are simulated. For case $F^+ = 1$, the actual PRF is 11233 Hz. Dimensionless time t^* is defined as t/t_0.

$$F^+ = \frac{PRF \cdot L_0}{U_\infty} \tag{1}$$

2.2. Flow conditions

Table 2 presents the freestream conditions utilized in numerical investigations that coincide with the test conditions of our supersonic Ludwieg tube with a Mach number of 4. We will conduct the corresponding experiments in future studies. Fully laminar flows are expected based on the relatively low unit Reynolds number of 7.8×10^6 m^{-1}.

Table 2 Freestream conditions

M_∞	Re_∞ (1 m^{-1})	p_∞ (Pa)	U_∞ (ms^{-1})	ρ_∞ (kgm^{-3})	T_∞ (K)
4.0	7.8×10^6	1126	674	0.055	70.7

3. Numerical methodology

3.1. Plasma model

A one-zone inhomogeneous phenomenological plasma model[27] of surface NSDBD is adopted in this study to predict the key discharge parameters, such as the plasma length, gas heating energy E_h for a single pulse per unit spanwise width, and its spatial distribution. By integrating

the propagation velocity with the pulse rising time τ_r, the plasma length L_D is estimated as a function of the peak voltage V and τ_r[27]. Here, the propagation velocity is acquired by curve fitting of the data, and its change with the voltage rise rate is estimated by the self-similar NSDBD model[28]. The energy input per unit spanwise width per pulse E_{in} is assumed to be a function of V and pulse repetition rate f obtained by curve fitting of the experimental data[29] as:

$$E_{in}(V,f) = \frac{(0.35215 - 0.14986 \times 0.99811^{f})}{(0.35215 - 0.14986 \times 0.99811^{10})}(0.18517V^0 - 0.0610V^1 + 0.00567V^2) \quad \textbf{(2)}$$

where E_{in} is in units of mJ·cm^{-1} and V is in kV. Therefore, E_h can be defined as:

$$E_h = \eta_h \cdot E_{in}(V,f) \quad \textbf{(3)}$$

where η_h is the efficiency of the energy input converted to gas heating. According to the work of Nudnova et al.[20, 30], during the discharge phase the rate of energy conversion is much smaller and can be estimated as 35±5% from the total discharge energy. Accordingly, the gas heating efficiency η_h is estimated as 35% during the discharge phase in this study.

The spatial distribution of the gas heating energy density $ED_h(x, y)$, defined as Eq. 4, can be obtained according to the averaged emission intensity ($EI(x/L_D, y/h)$) studied experimentally by Maryia et al.[20]. Note that it is assumed that the energy used to heat the gas is proportional to the intensity of the radiation.

$$ED_h(x,y) = E_h(V,f) \cdot \frac{EI(x/L_D, y/h)}{EI_T} \quad \textbf{(4)}$$

Here, EI_T is the integral value of the distribution function EI, and h is the thickness of plasma according to experiments. Therefore, the power density distribution p_h, serving as a heating source within the governing equations, is hereby defined as

$$p_h(x,y) = ED_h(x,y)/\tau_h \quad \textbf{(5)}$$

where τ_h is a characteristic heating time. Unfer et al.[31] proposed a two-dimensional self-consistent numerical model of the discharge and gas dynamics to simulate the fast gas heating process, and a three-species physical model was presented by Wang[32] to predict the energy and forces. Montello et al.[33] indicated that the fast heating process in air occurs on a time scale (~100 ns) shorter than the characteristic acoustic time scale. Zheng et al.[34] found that a larger τ_h results in a delay of shock initiation and consequently a shock slightly lagging behind that with a smaller τ_h. In this study, τ_h is taken to be 350 ns, which was reported to be the best quantitative agreement with experiments[34].

3.2. Compressible Navier–Stokes equations

The governing equations are the 2D compressible Navier–Stokes equations for a calorically perfect gas written in the following conservation form[2, 34]:

$$\frac{\partial U}{\partial t}+\frac{\partial F}{\partial x}+\frac{\partial G}{\partial y}=\frac{\partial F_v}{\partial x}+\frac{\partial G_v}{\partial y}+S_h \tag{6}$$

where

$$U=\begin{pmatrix}\rho\\ \rho u\\ \rho v\\ \rho e\end{pmatrix}, F=\begin{pmatrix}\rho u\\ \rho u^2+p\\ \rho uv\\ (\rho e+p)u\end{pmatrix}, F_v=\begin{pmatrix}0\\ \tau_{xx}\\ \tau_{xy}\\ u\tau_{xx}+v\tau_{xy}-q_x\end{pmatrix},$$
$$G=\begin{pmatrix}\rho v\\ \rho uv\\ \rho v^2+p\\ (\rho e+p)v\end{pmatrix}, G_v=\begin{pmatrix}0\\ \tau_{xy}\\ \tau_{yy}\\ u\tau_{xy}+v\tau_{yy}-q_y\end{pmatrix}, S_h=\begin{pmatrix}0\\ 0\\ 0\\ p_h\end{pmatrix} \tag{7}$$

In these expressions, ρ, p, u, and v are the density, pressure, and x and y velocity components, respectively. τ_{ij} is the shear stress tensor modeled under the assumption of a Newtonian fluid and the Stokes hypothesis, and q is the vector of heat conduction modeled according to Fourier's law. Sutherland's law is used to evaluate the dynamic viscosity. The specific heat ratio γ and Prandtl number Pr are set to 1.4 and 0.72, respectively. The effect of the discharge on flow is represented as a heating source p_h in the energy equation predicted by the plasma model[27], as described in Eq. (5). Note that it is set to zero outside the heating time.

The numerical simulations in this study are performed using a multiblock parallel finite-volume CFD code called PHAROS, which has been successfully applied to supersonic/hypersonic flows over capsule, double-cone, hollow-cylinder/flare[35], and double-wedge configurations[36]. The inviscid fluxes are calculated using the modified Steger–Warming scheme, which can stably capture strong shocks while maintaining sufficient viscous resolution in the boundary layers[37]. The scheme is then extended to a higher order by monotonic upstream-centered schemes for conservation law reconstruction[38]. The viscous fluxes are calculated using a second-order central difference. An implicit line relaxation method[39] is utilized for pseudo time stepping to obtain a steady flow before activation, and a second-order implicit scheme[40] is utilized for time marching in unsteady flow after activation[41].

3.3. Vortex transport equation

After the activation of the plasma actuator, the coexistence of induced compression waves, near-wall residual heat, and induced vortices indicates a complicated flow field. To analyze the formation of induced vorticity after the interaction of freestream and thermal perturbation, the vorticity transport equation is introduced, which is derived from the Navier–Stokes momentum

equation. While the presence of electrodes can induce some three-dimensional flow, particularly due to the uneven distribution or configuration along spanwise, the current utilization of a straight strip electrode configuration can be regarded as quasi-two-dimensional. Therefore, the flow is considered compressible, viscous, and two-dimensional. The vorticity transport equation is shown accordingly as:

$$\frac{\partial \omega_z}{\partial t} = -(\vec{u} \cdot \nabla)\omega_z - \omega_z(\nabla \cdot \vec{u}) + \frac{1}{\rho^2}\nabla\rho \times \nabla P + \nabla \times \left(\frac{\mu}{\rho}\nabla^2\vec{u} + \frac{1}{\rho}\frac{\mu}{3}\nabla(\nabla \cdot \vec{u})\right) \quad (8)$$

This form includes four vorticity source terms on the right-hand side of Eq. (8), encapsulated as the convection term, compression–expansion term, baroclinic term, and viscous term. Note that the term $(\vec{\omega} \cdot \nabla)\vec{u}$ is zero for a 2-D form, which describes the stretching or tilting of vorticity caused by the velocity gradient. The term $-(\vec{u} \cdot \nabla)\omega_z$ represents the vorticity migration rate, corresponding to the vorticity transport by convection. Term $-\omega_z(\nabla \cdot \vec{u})$ is the vorticity variation due to the change in the fluid microgroup volume caused by the compression or expansion (dilatation) effects. The term $\frac{1}{\rho^2}\nabla\rho \times \nabla P$ accounts for changes in vorticity when the density and pressure do not satisfy the barotropic relationship. The last term corresponds to the fluid viscosity effects on the diffusion of vorticity.

3.4. Computational details

3.4.1 Mesh resolution and boundary conditions

In the following investigation and discussion in Section 4, the formation of induced flow on a flat plate in quiescent air is initially studied. To validate the plasma model, the conditions based on our experiments[22] are selected for comparison with numerical simulations. The computational domain is 40 mm and 20 mm with a grid resolution of 1000 × 500 in the *x* and *y* directions, respectively. The plasma region starts at $x = 0$. The peak voltage, atmospheric pressure, and temperature are set at 35 kV, 101325 Pa, and 300 K, respectively. Then, the mesh domain for the simulation over the compression corner is shown in Fig. 2 (a). The mesh close to the wall remains orthogonal to the wall, as shown in Fig. 2 (b).

The boundary conditions are specified as follows: freestream conditions are prescribed at the upper and left boundaries. A simple extrapolation outflow condition is used at the exit boundary. For the no-slip wall, isothermal conditions are specified with a wall temperature of 297 K.

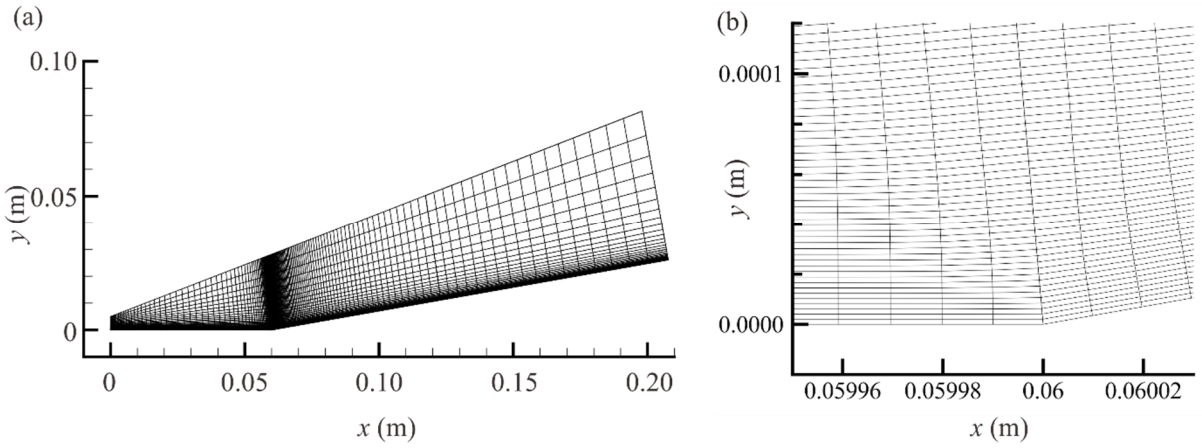

Fig. 2. (a) Mesh domain of the total simulation region for a compression corner (each 10th point is shown); (b) the grid distribution at the corner (Grid 0.72 × 10^6 (1600 × 450)).

3.4.2 Convergence study

To build confidence in the simulations, the independence of time steps and grid numbers are investigated to ensure convergence and stability. The distributions of dimensionless overpressure P/P_∞ at $x/L_0 = 0.7$ for case C6 ($L_p/L_0 = 0.67$, $V = 50$ kV, see Table 1) at 2 μs after a single activation with grid refinement are shown in Fig. 3 (a). Four grid numbers of 0.18 × 10^6 (800 × 225), 0.36 × 10^6 (800 × 450), 0.72 × 10^6 (1600 × 450), and 1.44 × 10^6 (1600 × 900) are used under the same time step (0.2 ns). The meshes are clustered near the leading edge, corner, and wall, with the mesh spacing at the wall being 1 × 10^{-6} m for all four cases, yielding a nondimensional wall distance of $y^+_{wall} \approx 0.3$. The present simulations reveal that the pressure distributions of grid schemes 0.72 × 10^6 and 1.44 × 10^6 are not very different, with the two-dimensional flow fields being nearly identical for both cases. In addition, four different time steps of 0.1, 0.2, 0.5, and 1 ns under the same grid cells (a total of 0.72 × 10^6) are used to validate time step independence. The changes in overpressure with time steps are shown in Fig. 3 (b). The sensitivity of time steps to overpressure is relatively limited[42]. To ensure the convergence of the simulation and save computing resources, the mesh scheme with a total number of 0.72 × 10^6 grids and a time step of 0.2 ns is selected for all subsequent simulations in this article.

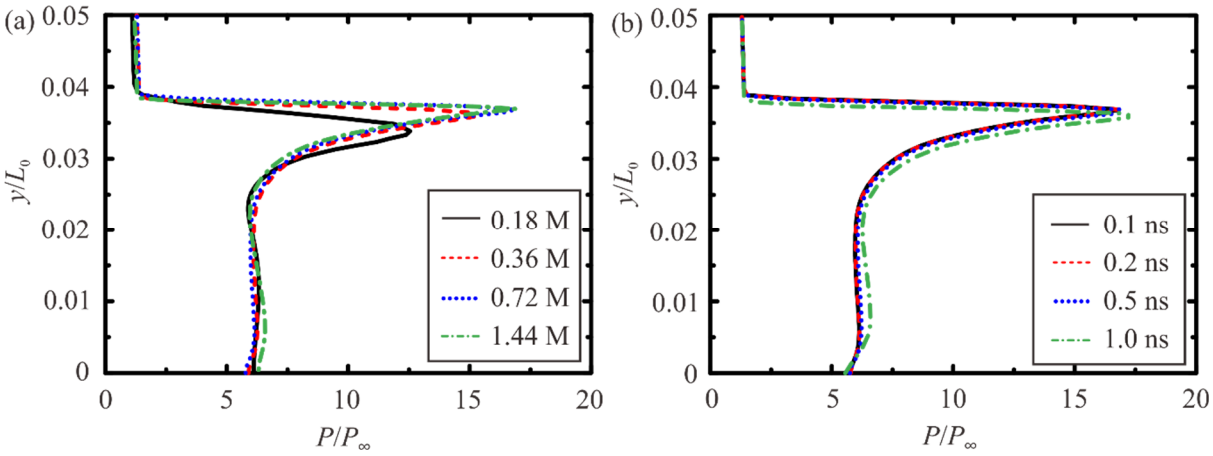

Fig. 3 The distributions of dimensionless overpressure 2 μs after activation located at x/L_0 = 0.7 with a freestream of M_∞ = 4 with the change in (a) grid cells (time step fixed at 0.2 ns) and (b) time steps (grid cell fixed at 0.72 × 10^6, 1600 × 450). The activated location is L_p/L_0 = 0.67 and V = 50 kV.

4. Results and discussion

4.1. Induced flow of NSDBD in quiescent air on a flat plate

An induced shock wave is one of the main characteristics of NSDBD, which is demonstrated in Fig. 4 with experimental and numerical schlieren images for the case of 35 kV actuation. The shock wave consists of a semicylindrical and a planar shock, which is generated by a rapid increase in pressure due to the high energy density of the discharge. The semicylindrical shock expands from the alignment line of the electrodes (discharge streamer head) and is followed by the planar shock propagating upward parallel to the discharge streamers associated with the gas heating in the discharge. The current numerical results of induced shock formation and flow evolution under NSDBD actuation are consistent with previous research[43, 44]. The induced shock quickly attenuates to a compression wave after several microseconds. This typically occurs prior to the shock front propagating 2 mm vertically toward the wall[22, 44]. Undoubtedly, the attenuation process is closely linked to the discharge parameters, including peak voltage and dielectric material. In this section, we only discuss the case when it attenuates to a compression wave. In Fig. 4, the position of the compression wave exhibits a high degree of consistency with the experimental observations. This consistency serves as an indication of the overall accuracy of the plasma model in predicting the propagation speed of the compression wave. Furthermore, it indirectly supports the reasonableness of the estimated gas heating energy. The numerical results indicate that the length of the planar shock in the simulations is slightly longer compared to the observations in the experiment (in Fig. 4). This disparity can

be attributed to various factors, such as the length of the electrodes, the presence of dielectric material, and other parameters that influence the size of the gas heating region, subsequently affecting the length of the planer shock. The current plasma model does not explicitly consider the dielectric material, thickness, and electrode size, because these factors insignificantly impact the estimation of discharge energy. It is reasonable for the model to focus on parameters like discharge voltage and frequency, which have a substantial influence on discharge energy estimation, as evidenced by the comparison under the same voltage in Fig. 4.

The interaction between the freestream and induced shock/compression waves is presented as a distortion of streamlines behind the shock front. This perturbance has little contribution to the changes in the flow field when the induced shock/compression waves have moved outside the plasma region. To clarify the influence of this perturbation, the unsteady pressure difference caused by the rapid compression above the flat plate at 5, 10, 20, and 30 μs after a pulsed discharge at $x = 0$ is studied, shown in Fig. 5. The perturbation caused by the induced compression wave is distributed in a thin region and quickly disappears after the induced compression wave propagates, which exhibits a localized and transient nature. The force was estimated by the integration of about 300 mN/m at 30 μs, which is on a similar order of magnitude in many publications[45, 46]. Notably, the thrust magnitude depends on various factors, including the voltage magnitude, electrode configuration, voltage type (alternating current or nanosecond pulse), etc.

Upon plasma generation, residual heat, caused by the gas heating, rapidly deposits in the discharge region and transfers to the surrounding air, creating a hotspot area that is completely decoupled from induced shock/compression waves marked by the dotted line in Fig. 4. Each pulse intensifies the heating in this region, and the heat thermally expands to the vicinity. The rapid gas heating is mainly caused by the reactions of predissociation of highly excited electronic states of oxygen molecules, the reactions of quenching of excited atoms $O(^1D)$ by nitrogen molecules, as well as vibrational-translational relaxation reactions[47]. For the cases examined in this study, utilizing voltages of 25 kV and 35 kV, the total input energy per pulse E_{in} was estimated to be 2.17 mJ/cm and 11.17 mJ/cm, respectively, using Eq. (2). Correspondingly, the heating power density p_h was determined to be 2.17 kW/cm and 11.17 kW/cm. Momentum migration resulting from the accumulation of residual heat plays a significant role in withstanding downstream adverse pressure gradients, which is supposed to be the control mechanism in flow control. At the same time, under the body force caused by the strong electric field, ionized particles migrate toward the dielectric surface. However, the movement of the thermal fluid is much slower than the heat deposition, as the effective time of

the electric field is short, which is usually on the order of nanoseconds for each pulse. Therefore, the present numerical study disregards the influence of the interaction of ionic wind due to the extremely short effective time of the body force caused by the plasma.

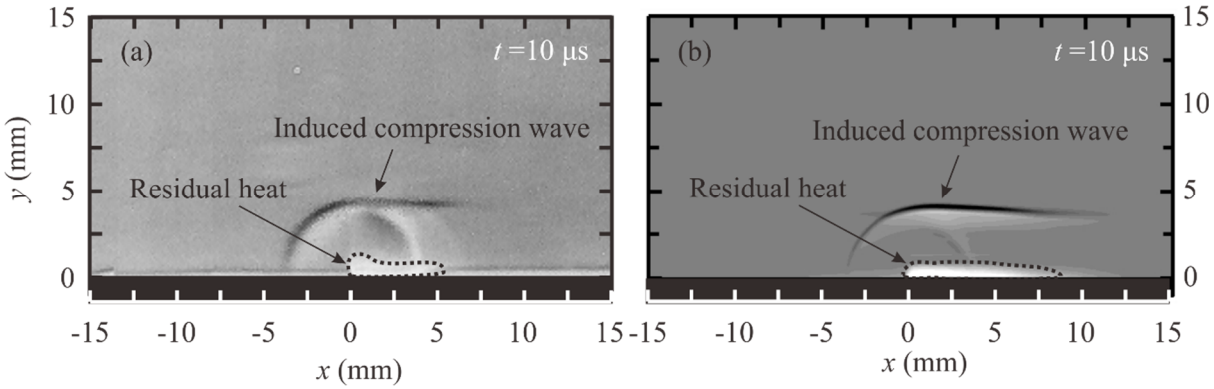

Fig. 4. Schlieren images showing the induced compression wave structures and the residual heat under a 35 kV actuation voltage from (a) the experiment reported by Chen et al.[22] and (b) the numerical simulation in this study.

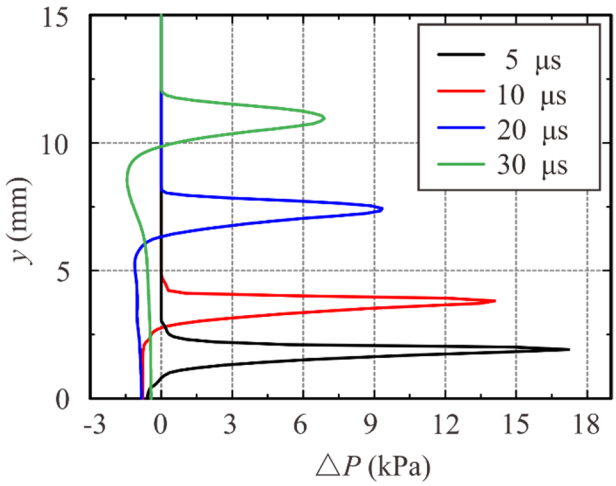

Fig. 5. Pressure difference caused by the compression wave above the flat plate at 5, 10, 20, and 30 μs after a pulsed discharge at $x = 0$ under 35 kV.

To further examine the induced vortex resulting from interaction with the freestream, the vorticity transport function is initially utilized to analyze the induced vorticity of a discharge on a flat plate in the absence of a freestream. Fig. 6 illustrates the contours of the vorticity and corresponding terms in the vorticity change rate after the activation time at 5 μs when the induced shock has propagated a certain distance away from the plasma region. As clearly illustrated in Fig. 6 (a)(b), the induced vorticity and its change rate by NSDBD are primarily concentrated in two regions: the induced compression wave region and the plasma region (heat emission region). By comparing each term that constitutes the vorticity change rate, it can be

found that violent vorticity changes resulting from convection (see Fig. 6(c)) and dilatation (see Fig. 6(d)) occur at the induced compression wave region, while those resulting from baroclinicity (see Fig. 6(e)) and viscosity (see Fig. 6(f)) occur near the plasma region. Therefore, the vorticity caused by the viscous term is primarily concentrated in the near-wall region (usually $y \sim 0.05$ mm, marked by the dashed frame in Fig. 6 (f)), whereas the vorticity caused by the baroclinic term is primarily concentrated in the plasma region (usually $y \sim 1$ mm, marked by the dashed frame in Fig. 6 (e)). This implies that the induced compression wave results in local fluid volume changes and convection, thereby altering the vorticity primarily confined to the thin layer of the induced compression wave. In the plasma region, residual heat induces fluid baroclinicity, which subsequently triggers thermal convection, leading to a substantial alteration in vorticity. As there is no freestream, vorticity changes caused by heat convection within the plasma region occur inconspicuously when compared to those within the induced compression wave region.

Although the viscosity dominates the vorticity generation in the near-wall region, the convection is still a factor in vorticity change in this region (see Fig. 6 (c) dashed frame). To determine the cause of vorticity generation for the convection term in the near-wall region, Fig. 7 (c) provides a detailed illustration of this region. Note that for better visualization, the scales of the horizontal and vertical coordinates are set to be independent. It is clear that the streamwise velocity gradient along the normal direction (see Fig. 7 (b)), which is caused by the compression wave sweeping the surface to form an induced thin boundary layer, mainly contributes to the convection term in the near-wall region. The induced boundary layer is the main cause of vorticity by convection in the near-wall region.

Note that the induced vorticity within the plasma region (see Fig. 6 (a)) is distributed along the heat emission (see Fig. 7 (a)) between –8.7 mm and 17.4 mm, as estimated by the plasma model. However, the instantaneous vorticity change rate at 5 μs is primarily concentrated at the head of the heat emission region, as shown in Fig. 6 (b) at $-0.5 \text{ mm} < x < 3$ mm. This is because the fast heating is concentrated at the head of the discharge. The vorticity change rate increases significantly during the initial discharge stages throughout the emission region, leading to vorticity changes. Following the discharge, the residual heat dissipates rapidly at the discharge tail but not completely at the head. Thus, after a period of time, such as 5 μs in Fig. 6, the instantaneous change rate of vorticity is only concentrated at the filament head. This observation reaffirms that the residual heat primarily accounts for the vorticity change in the plasma region.

It is apparent that the vorticity in the plasma region is mainly induced by the instantaneous pressure rise resulting from discharge, which in turn triggers the misalignment of the pressure gradient and density gradient in the plasma region, followed by the vorticity transfer caused by the flow field convection near the plasma region. This section emphasizes that baroclinicity is the main cause of the induced vorticity by discharge in the quiescent air.

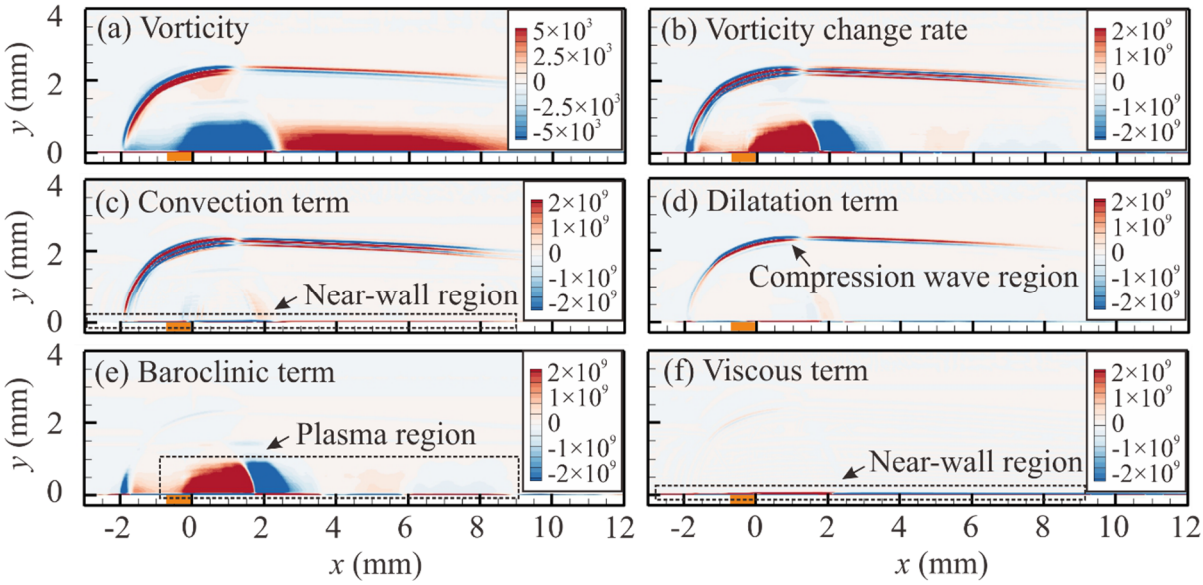

Fig. 6. Vorticity and relative term contours at 5 μs after a single pulse activation at 50 kV. (a) Vorticity; (b) vorticity change rate; (c) convection term; (d) dilatation term; (e) baroclinic term; (f) viscous term.

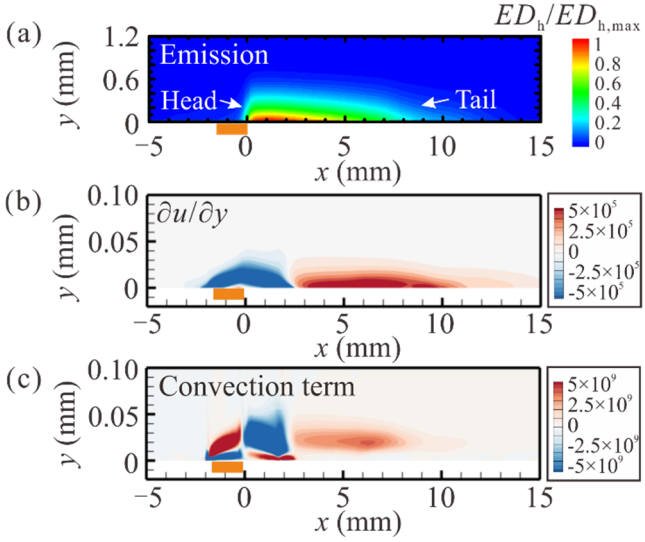

Fig. 7 (a) Heating source emission distribution at V = 50 kV; (b) streamwise velocity gradient along the y direction; (c) convection term in the near-wall region at 5 μs after a single pulse activation at 50 kV.

4.2. Large-scale separation over the supersonic compression corner

The compression corner is composed of a flat plate with a sharp leading edge, followed by a ramp. Fig. 8 illustrates the key features of a laminar-separated supersonic flow over the compression corner, indicating that the baseline flow in this study is a typical large-scale separation. The entire separation process can be described as follows. The boundary layer on the flat plate separates from the surface, caused by a sufficiently large pressure increase due to the ramp. It then reattaches to the downstream ramp, leading to a reattachment shock (RS). The separation shock (SS) and reattachment shock intersect at the triple point (TP). Beneath the separated shear layer, a recirculation bubble forms between the separation point (SP) and reattachment point (RP). The states of the recirculation bubble are intimately connected to the global stability of the flow. For instance, in the presence of global instability, 3-D streamwise streaks downstream of the reattachment can arise without any external disturbance. Therefore, a thorough examination of the recirculation bubble is imperative. In this study, the shear flow separates at $x/L_0 = 0.58$ and reattaches at $x/L_0 = 1.42$ with a nondimensional separation bubble length of $L_b = l_b/L_0 = 0.84$ and a vortex core at $x/L_0 = 1.09$, where l_b is the dimensional separation bubble length. The size of the recirculation bubble is heavily influenced by the deflection angle α, Mach number M_∞, Reynolds number Re_{L0}, and temperature ratio T_w/T_∞ of the incoming flow[48]. A scaled ramp angle α^* defined in Eq. 9 establishes a correlation of these parameters, which is determined by the characteristic scaling in the triple-deck theory[49, 50].

$$\alpha^* = \frac{\alpha \cdot Re_{L_0}^{1/4}}{C^{1/4} 0.332^{1/2} (M_\infty^2 - 1)^{1/4}} \tag{9}$$

$$C = \frac{\mu_w T_\infty}{\mu_\infty T_w} \tag{10}$$

Here, C is the Chapman–Rubesin parameter. The triple-deck theory is initially applied to predict the incipient separation, which has a scaled ramp angle α^*=1.57. With increasing α^*, the processes of flow separation and reattachment are no longer interconnected but are instead separated by a nearly constant pressure region (see Fig. 8(c)), forming a large-scale separation bubble. The pressure plateau is a significant characteristic of a large separation[51] and usually occurs when $\alpha^* \geq 2.5$. Korolev et al.[52] further confirmed that the scaled length of the separation region was linearly proportional to $\alpha^{*3/2}$ in a large-scale separation, which extends this theory to large-scale separation problems. As α^* further increases up to a critical value, the flow becomes globally unstable. A secondary eddy, even multiple eddies, appears in the recirculation region. Based on a global instability analysis by Hao et al.[2], the stability boundary prediction of the critical value α^* is 4.59 for the current flow conditions. In this study, the

scaled ramp angle α^* is 4.2, which is less than this critical value, implying that the baseline flow is globally stable.

The enlarged views with the vorticity contours in Fig. 8 (b) show the flow details of the recirculation region. Two streamwise velocity isolines at u/u_∞ = 0.9 and 0.1 are marked, covering the main part of the shear layer. The high-speed outer flow velocity decreases rapidly due to the adverse pressure gradient, forming a thin shear layer. Below the shear layer, the reverse streamwise velocity forms a reverse flow boundary layer near the ramp surface due to the viscosity, illustrated by the high vorticity region in Fig. 8 (b) red contours. The reverse streamwise velocity in the reverse boundary layer increases under the favorable pressure gradient, leading to a local shear stress minimum τ_2 on the surface (see Fig. 8 (d)). Then, the reverse streamwise velocity decelerates strongly. After it passes through the corner, it accelerates again, resulting in a local skin friction peak near the corner and another local shear stress minimum τ_1 on the surface. Note that when the local peak becomes positive, it indicates the emergence of secondary separation, and the flow has become globally unstable. The presence of two skin friction minima immediately before reattachment is the other characteristic feature of a large-scale separated region. In summary, as the first step in the study, the baseline flow is a typical large-scale stable laminar separated flow.

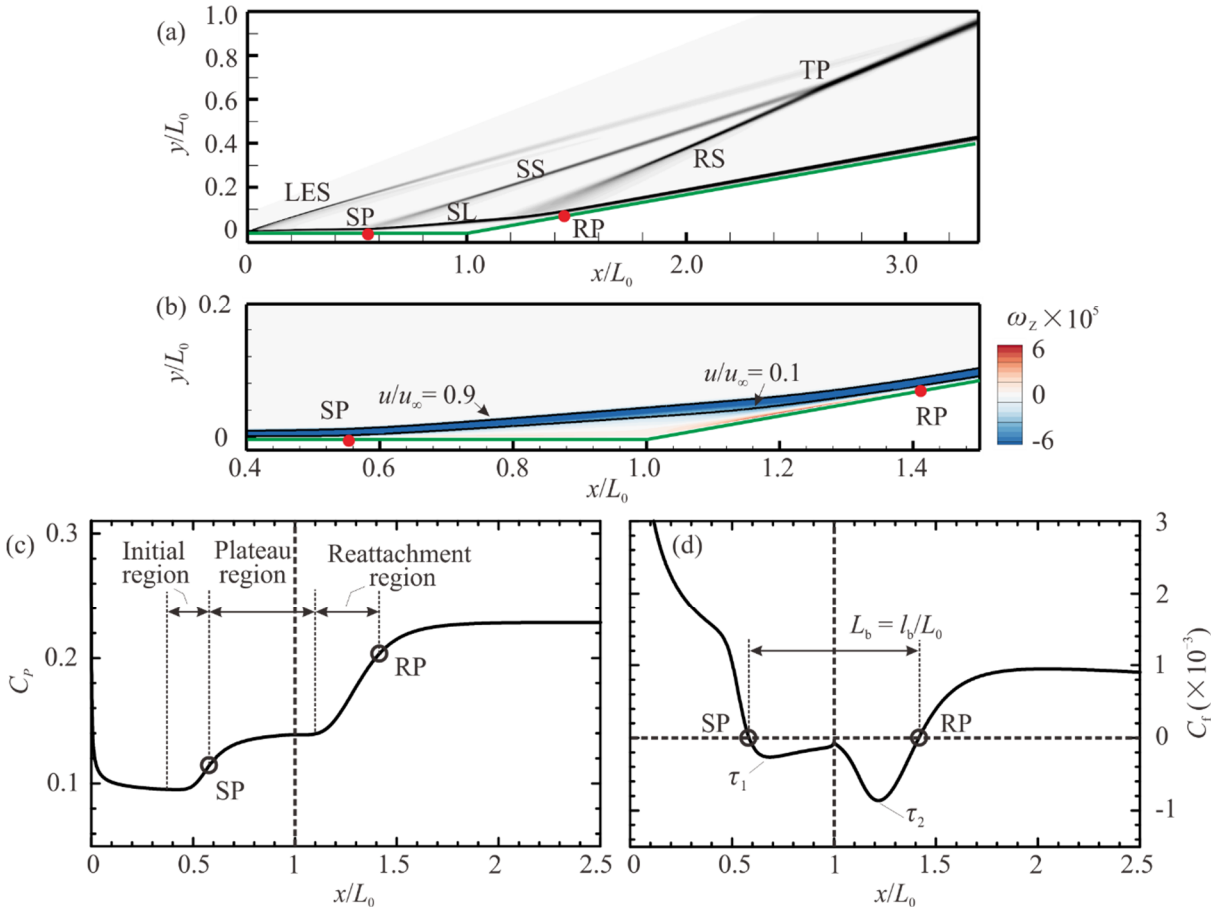

Fig. 8 Schematic of (a) the flow structures over a compression corner; (b) vorticity contours in the separation region; (c) surface pressure coefficient; (d) skin friction coefficient at $\alpha^* = 4.2$. Green solid line: the surface of the ramp. Circles: separation point and reattachment point. Here, LES represents the leading-edge shock, SS represents the separation shock, RS represents the reattachment shock, SL represents the shear layer, SP represents the separation point, RP represents the reattachment point, and TP represents the triple point.

4.3. Impact on the recirculation region

The pulsed repetitive frequency and applied voltage substantially impact the control effects, which can increase the energy in the discharge in a unit interval and a single pulse, respectively. Furthermore, the varied locations of activation can significantly influence the control performance, which can have diverse mechanisms contingent on the baseline flow structures. Here, we take the flow structures in the recirculation region to analyze the influence of cases with activation locations at L_p/L_0 = 0.33, 0.5, and 0.67, PRFs of F^+ = 1, 10, and 20 and applied voltages of 25 kV and 50 kV. The controlled flow will first enter a flow establishment state (when the induced flow revises the original flow structures from t^* = 0 to 1.5) and then enter a

quasi-stable state (when the main flow moves under continuous activation from t^* = 1.5 to 3.0). The flow establishment details will be discussed in Sections 4.4 and 4.5. The impacts on the recirculation region presented in this section are in the quasi-stable state. The structures of separated flows are illustrated by streamlines time-averaged from t^* = 1.5 to 3.0, together with contours of the nondimensional streamwise velocity increment $\overline{u'}/U_\infty$. The separation bubble sizes after periodic control are summarized in Table 3.

Table 3. The reduction in separation bubble length for simulated cases.

Case	C0	C1			C2			C3		
F^+	-	1	10	20	1	10	20	1	10	20
SP (x/L_0)	0.58	0.59	0.67	0.70	0.65	0.77	0.79	0.73	0.87	0.89
RP (x/L_0)	1.42	1.43	1.47	1.48	1.44	1.50	1.51	1.44	1.52	1.21
L_b/L_0	0.84	0.84	0.81	0.78	0.79	0.73	0.72	0.71	0.65	0.32
Reduction (%)	0	0.4	4.1	7.1	5.7	13.4	14.3	15.5	22.5	62.0
Case	C0	C4			C5			C6		
F^+	-	1	10	20	1	10	20	1	10	20
SP (x/L_0)	0.58	0.66	0.83	0.86	0.75	0.94	-	0.89	-	-
RP (x/L_0)	1.42	1.44	1.52	1.50	1.45	1.13	-	1.38	-	-
L_b/L_0	0.84	0.78	0.69	0.64	0.70	0.79	0	0.49	0	0
Reduction (%)	0	7.0	17.8	24.5	16.9	77.4	100	41.9	100	100

4.3.1. L_p/L_0 = 0.33 (cases C1 and C4)

The time-averaged separation flow structures and skin friction coefficient of cases C1 and C4, where the activation location is far away from the SP, are presented in Fig. 9. At F^+ = 1 (see Fig. 9 (a) and (d)), the bubble size slightly shrinks, and there is no obvious induced separation bubble. The origin of the induced separation bubble will be explained in the next section. The SP moves downstream slightly from x/L_0 = 0.58 to 0.59 and 0.67. The bubble length L_b decreases by 0.4% and 7.0%. Compared to single pulse control with the same location (0% for C1 and 5.0% for C4), the effectiveness of reducing the separation bubble exhibits a slight increase.

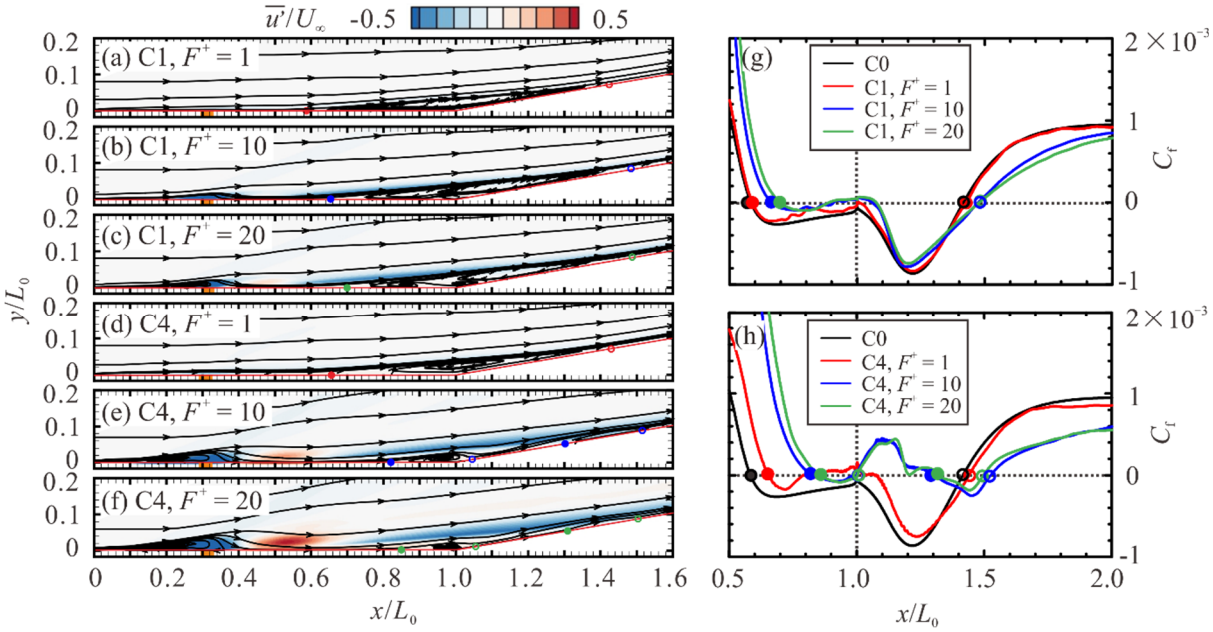

Fig. 9 Time-averaged contours of normalized streamwise velocity fluctuation ($\overline{u'}/U_\infty$) for cases C1 (25 kV) at (a) F^+ = 1; (b) F^+ = 10; (c) F^+ = 20; and cases C4 (50 kV) at (d) F^+ = 1; (e) F^+ = 10; (f) F^+ = 20 with streamlines superimposed in the quasi-stable state. Distributions of the time-averaged skin friction coefficient for cases (g) C1 (25 kV) and (h) C4 (50 kV). L_p/L_0 = 0.33. (SP: solid circle; RP: hollow circle)

In the cases of C1 at F^+ = 10 and 20 (see Fig. 9 (b) and (c), and Table 3), the main bubble length L_b is reduced by 4.1% and 7.1%, and an induced separation bubble appears upstream of the activation location (L_p/L_0 = 0.33). The velocity above the separation bubble decreases significantly, leading to the reduction of skin friction and surface pressure in the vicinity of RP on the ramp. The separation region is pushed downstream with a slight shrinkage. However, from the skin friction distribution, the separation bubble seems to remain in the same state, shown in Fig. 9 (g). As shown in Table 3, the suppression of the main separation bubble size is approximately the same for case C4 of F^+ = 1 (Fig. 9 (d)) and case C1 of F^+ = 20 (Fig. 9 (f)), but the energy consumption is quite different. Take case C1 at F^+ = 1 as a reference. The energy input (see Eq. (2)) of case C4 at F^+ = 1 is 5.1 times that of case C1 at F^+ = 1, whereas it is 20 times for the case of C1 (F^+ = 20). This implies that when the activation location is far upstream from the SP, improving the applied voltage is more effective in reducing the separation bubble than increasing the PRF on the suppression of bubble length.

For cases C4 at F^+ = 10 and 20 (see Fig. 9 (e) and (f)), two segments of separation can be observed, which is also seen in Fig. 9 (h). The main bubble near the corner is reduced, but under a high adverse pressure gradient downstream, the flow will be separated again on the

ramp surface and subsequently reattached. The bubble length is calculated from the first SP to the last RP to unite it in all cases. After the control, the total bubble length L_b is reduced by 17.8% and 24.5%, and the induced separation bubble further expands upstream of the activation location due to the high activation frequency. From the contours of the normalized streamwise velocity fluctuation ($\overline{u'}/U_\infty$) in Fig. 9, it can be seen clearly that the velocity downstream of the activated location for cases C4 at F^+ = 10 and 20 increases significantly compared to other cases. Furthermore, the SP is pushed downstream by increasing the PRF because the pressure increases significantly upstream of the original SP.

4.3.2. L_p/L_0 = 0.5 (cases C2 and C5)

The time-averaged separation flow structures of cases C2 and C5 are presented by the streamlines in Fig. 10. The activation location is at L_p/L_0 = 0.5, which is slightly upstream of the original SP (case C0). The contours of the dimensional streamwise velocity increment $\overline{u'}/U_\infty$ are also plotted. The effectiveness of reducing the separation bubble at this activation location is markedly higher than L_p/L_0 = 0.33. In the cases of C5 at F^+ = 10 and 20 (see Fig. 10 (e) and (f)), the main separation bubble is significantly contracted. It can be seen clearly that the velocity in the boundary layer grows significantly in these two cases. In Fig. 18 (b) (blue and green lines), the surface pressure arises upstream of the corner and has a smaller adverse pressure gradient on the ramp, which favors separation suppression. These simulation results indicate that it is possible to completely eliminate the flow separation around the supersonic compression corner. By increasing F^+ from 10 to 20 in case C2, the skin friction increases due to a larger entrained velocity but to a limited extent (see Fig. 10 (g) blue and green lines). A comprehensive description of the surface friction analysis is presented in Section 4.5. In addition, the effectiveness of reducing the separation bubble only increases by 0.9%. In contrast, a larger separation bubble is induced upstream of the activation location (same in cases C2 and C5) with increasing F^+. This indicates that there is a critical F^+ that can eliminate the main separation and have a minimum side effect of the induced bubble at the same time. Similar to cases C1 (F^+ = 20) and C4 (F^+ = 1), cases C2 (F^+ = 20) and C5 (F^+ = 1) exhibit the same performance. This implies that improving the applied voltage is also more energy effective than increasing the PRF at L_p/L_0 = 0.5, similar to the cases at L_p/L_0 = 0.33.

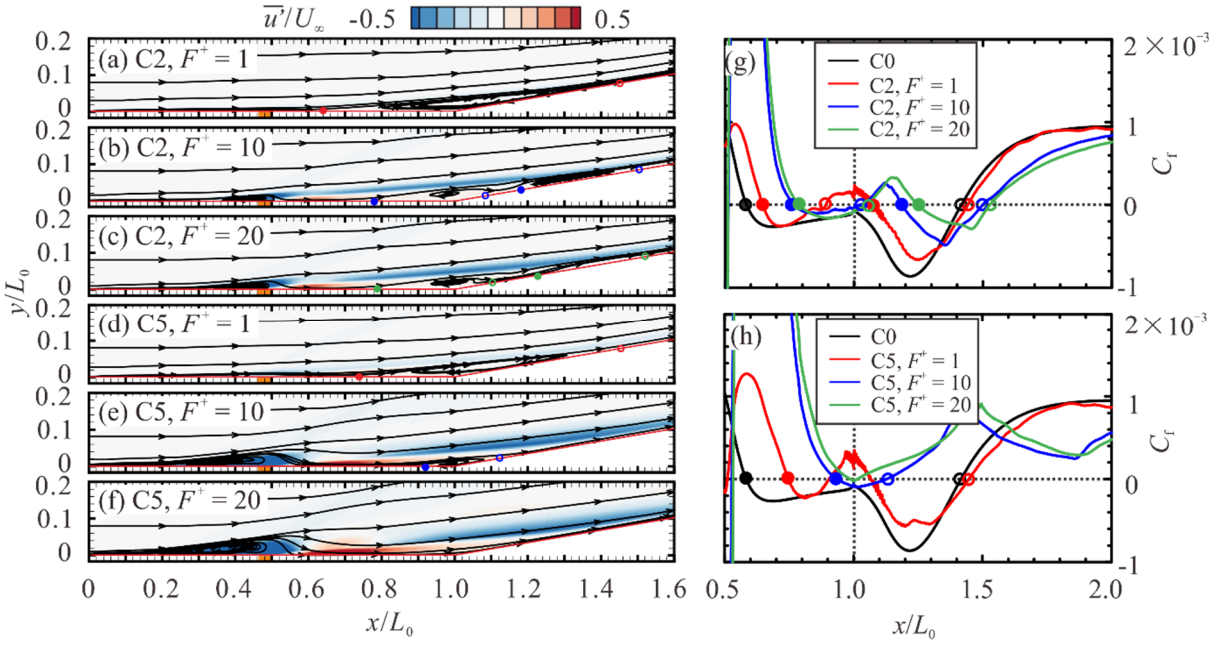

Fig. 10 Time-averaged contours of normalized streamwise velocity fluctuation ($\overline{u}'/U_\infty$) for cases C2 (25 kV) at (a) F^+ = 1; (b) F^+ = 10; (c) F^+ = 20; and case C5 (50 kV) at (d) F^+ = 1; (e) F^+ = 10; (f) F^+ = 20 with streamlines superimposed in the quasi-stable state. Distributions of the time-averaged skin friction coefficient for cases (g) C2 (25 kV) and (h) C5 (50 kV). L_p/L_0 = 0.5. (SP: solid circle; RP: hollow circle)

4.3.3. L_p/L_0 = 0.67 (cases C3 and C6)

Fig. 11 shows the time-averaged separation flow structures of cases C3 and C6 by the streamlines. The activation location is at L_p/L_0 = 0.67 downstream of the original SP (case C0). The contours of the dimensional streamwise velocity increment $\overline{u}'/U_\infty$ are also plotted. The control effectiveness of reducing the separation bubble at this activation location shows the best performance compared to the previous two actuation locations at the corresponding F^+. Similar to cases C5, cases C6 at F^+ = 10 and 20 will totally eliminate the separation, it also can be seen in Fig. 11 (h) that the skin friction is always positive near the corner, but the induced bubble seems to enlarge. It should be noted that case C3 at F^+ = 20 also almost suppresses the main bubble. Only a small separation exists on the ramp from 0.9 to 1.2 (see Fig. 11 (c)). This indicates that applying a lower voltage but with a high activation frequency can also eliminate the bubble. However, the choice of activation location becomes the key factor. Compared to case C2 (L_p/L_0 = 0.50) at F^+ = 20, the effectiveness of reducing the separation bubble increases from 14.3% to 62.0% in case C3 (L_p/L_0 = 0.67) at F^+ = 20. Similarly, taking the C1 case at F^+ = 1 as the reference, the power consumption of case C3 at F^+ = 20 is 20 times that of the reference case. Comparatively, in case C5 at F^+ = 10, it is approximately 50 times. This result

again implies that the activation location plays an important role in supersonic compression corner flow control.

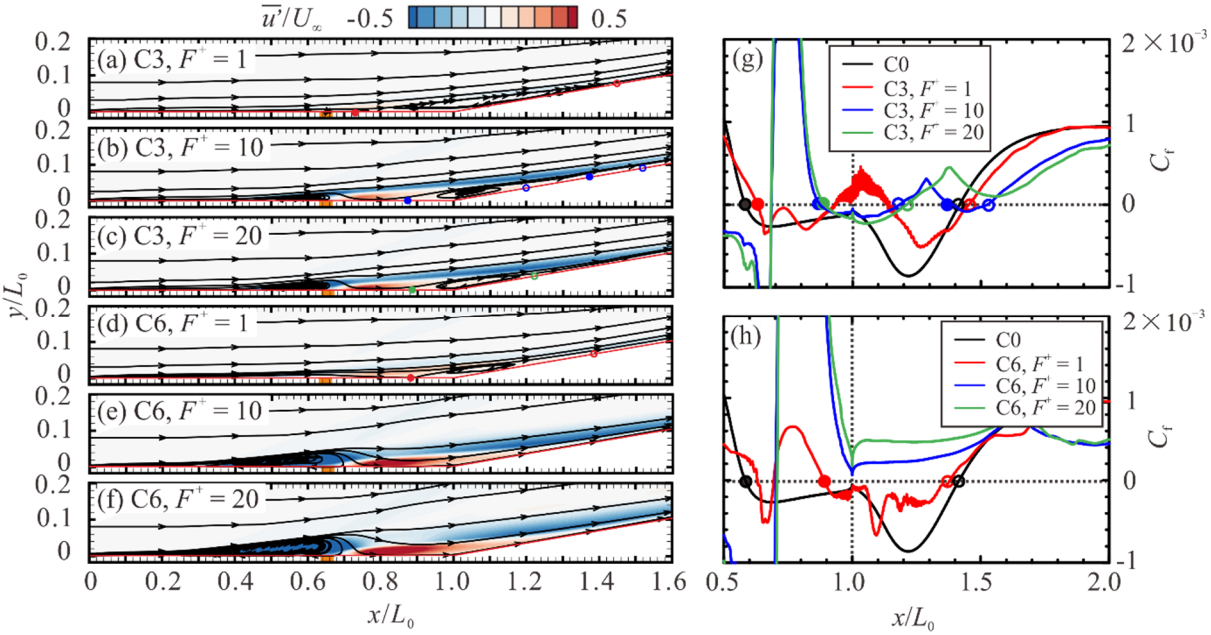

Fig. 11 Time-averaged contours of normalized streamwise velocity fluctuation ($\overline{u}'/U_\infty$) for cases C3 (25 kV) at (a) F^+ = 1; (b) F^+ = 10; (c) F^+ = 20; and case C6 (50 kV) at (d) F^+ = 1; (e) F^+ = 10; (f) F^+ = 20 with streamlines superimposed in the quasi-stable state. Distributions of the time-averaged skin friction coefficient for cases (g) C3 (25 kV) and (h) C6 (50 kV). L_p/L_0 = 0.67. (SP: solid circle; RP: hollow circle)

4.4. Discussion of the control mechanism

As per prior investigations, NSDBD primarily alters the flow structures via the interaction between the high-temperature and high-pressure residual heat area and the mainstream. Based on the results mentioned above, the interaction can lead to momentum transfer. This section provides a detailed discussion of the interaction between the induced flow and the main flow after discharge to further comprehend the control mechanism.

The streamwise velocity profiles of cases with different activated locations at L_p/L_0 = 0.33, 0.5 and 0.67 are presented in Fig. 12. under the same input energy at F^+ = 10 and V = 50 kV. This indicates a significant momentum exchange between the boundary layer and the upper flow, accompanied by a notable decrease in momentum above the boundary layer. A prominent negative velocity defect is observed in the baseline case, which represents a typical separated flow. At a location immediately downstream of the activation, the velocity near the wall increases, benefiting from the momentum supplement provided by the upper high-speed fluid. Downstream of the corner at x/L_0 = 1, the velocity increment decreases, but a noticeable

decrease in velocity above the original shear layer is observed. This suggests that momentum exchange mainly occurs downstream of the excitation, and the velocity deficit above the boundary layer continues downstream of the RP.

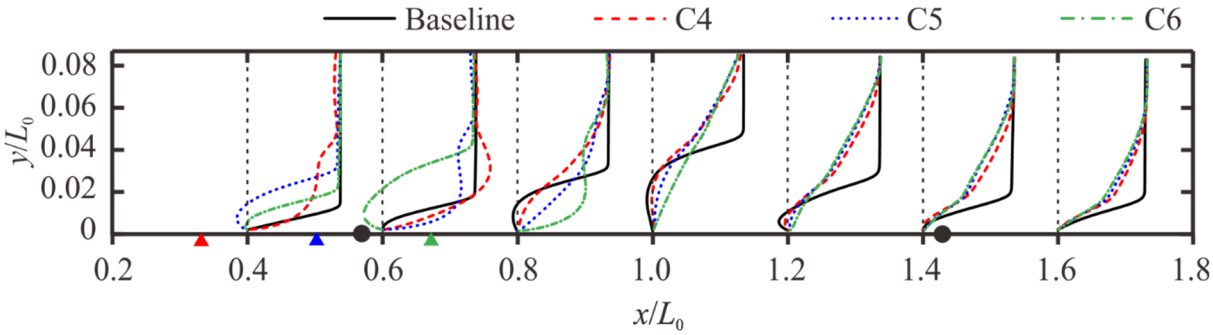

Fig. 12 Time-averaged streamwise velocity profiles over the ramp surface of cases L_p/L_0 = 0.33, 0.5 and 0.67 at F^+ = 10 and V = 50 kV. Triangular mark: activated location; Circular mark: original SP and RP.

This result implies momentum exchange upstream and downstream of the initial shear layer, with high-speed fluid carrying more momentum being transferred to the separation region, which significantly fills the velocity deficit in the boundary layer. This improves the flow's ability to resist an adverse pressure gradient, leading to a reduction in the separation bubble. To further analyze the cause of momentum migration, a vorticity analysis is conducted, focusing on the residual heat region. Fig. 13 shows the decomposition of the vorticity change rate at three different time instants at t^* = 0.022, 0.067, and 2.49 for the case of L_p/L_0 = 0.5, F^+ = 10, and V = 50 kV (case C5). Following the initiation of the control (2 μs, t^* =0.022), significant vorticity is produced by both compressibility (see Fig. 13 (b4)) and baroclinic effects (see Fig. 13 (b5)). The convection, driven by the incoming flow, leads to a considerable transport of vorticity change (see Fig. 13 (b3)), while the vorticity caused by viscosity is present adjacent to the wall (see Fig. 13 (b6)). The local pressure surge of discharge causes the upstream boundary layer to separate, which forms an induced separation shock (ISS), while the induced shock/compression waves (IS) generated by the discharge propagate and distort under the interaction with the incoming freestream. The maximum vorticity is generated at the junction of the ISS and IS. Subsequently (6 μs, t^* = 0.067, still before the secondary pulse), the vorticity changes caused by compressibility migrated upstream, leading to further expansion to form an induced separation vortex. The external high-speed fluid will be drawn to reattach the induced separation flow to the surface downstream of the activation location under a local favorable pressure gradient (see Fig. 18, where the local pressure rise in the residual heat region). It is worth noting that the induced shock gradually decouples from the residual heat

region, and its influence on the main separation downstream can be disregarded. After multiple pulses, the flow field approaches a quasi-stable state. Fig. 13 (d1) to (d6) displays the instantaneous situation before the 25th pulse (t^* = 2.49), where the induced separation bubble stably exists upstream of the plasma region and forms a stable induced separation shear layer caused by convection and compressibility. This result is more evident in the time-averaged results shown in Fig. 14 (a). Then, the involvement of the high-speed fluid generates significant shear forces in the reattached boundary layer, which appear to be caused by four mechanisms (convection, baroclinic, dilatation, and viscous terms) simultaneously. Notably, the vorticity changes caused by the baroclinicity seem to propagate to the downstream region (marked by an ellipse in Fig. 13 (d5)), with this region (x/L_0 ~ 0.8) corresponding to the area in the instantaneous temperature field (see Fig. 15 (j)) where the temperature gradient undergoes the most significant change. This indicates that the baroclinicity generated by the residual heat continues to produce vorticity downstream as the residual heat moves downstream. Considering the results in Section 4.1, it can be deduced that the generation of vorticity in the plasma region is primarily induced by the baroclinicity of residual heat. Under the interaction of supersonic freestream, convection, compressibility of the fluid element, and baroclinicity of the residual heat region jointly lead to the formation of the separation vortex, ultimately facilitating momentum migration.

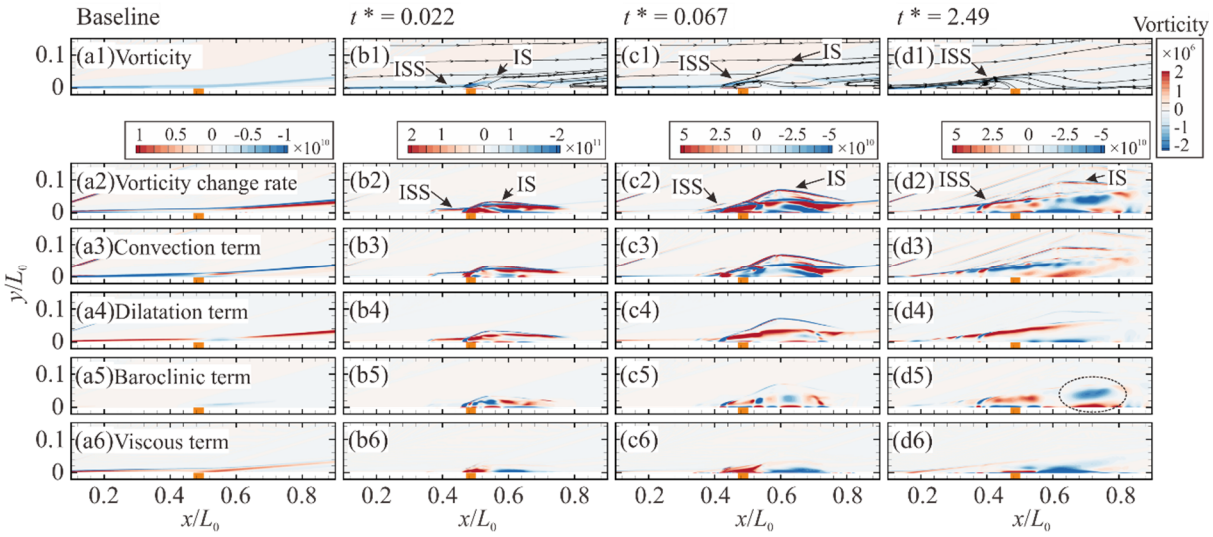

Fig. 13 The vorticity, vorticity change rate and decomposition of the convection term, compression–expansion term, baroclinic term, and viscous term of the baseline case (a1)-(a6) and three different instantaneous cases of L_p/L_0 = 0.5, F^+ = 10, and V = 50 kV at t^* = 0.022 (b1)-(b6), 0.067 (c1)-(c6), and 2.49 (d1)-(d6). The decomposition of the vorticity change rate at a typical time instant shares the same contour legend levels.

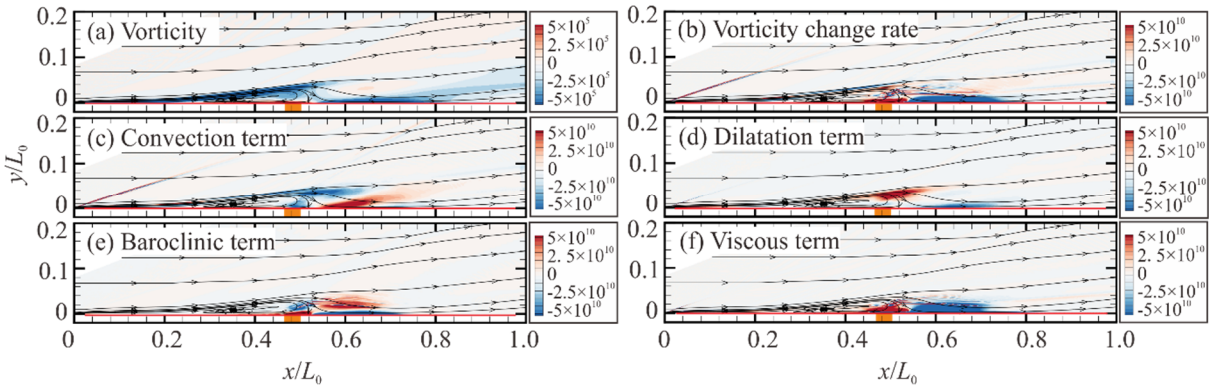

Fig. 14 Contours of time-averaged vorticity and relative terms in the case of L_p/L_0 = 0.5, F^+ = 10, and V = 50 kV. (a) Vorticity; (b) vorticity change rate; (c) convection term; (d) compression–expansion term; (e) baroclinic term; (f) viscous term.

To further investigate the flow interactions that lead to the suppression of the separation bubble after control, the instantaneous flow field is analyzed. Taking case C5 at L_p/L_0 = 0.50 and F^+ = 10 as an example, the normalized streamwise velocity contours overlaid with streamlines are illustrated in Fig. 15 (a)-(e). At t^* = 0.1, at the beginning of the first discharge, the induced vortices form the initial separation bubble near the original separation point of the boundary layer, and the high-speed external fluid is entrained into the original separation region. Subsequently, at t^* = 0.5 (see Fig. 15 (b), after the fifth pulse), when the entrained fluid passes through the corner, the separation bubble is pushed downstream due to the continuous entrained fluid. Then, the high-speed fluid impacts the ramp and further compresses the bubble. Although the original shear layer is totally destroyed, the adverse pressure region still occurs near the corner where the surface pressure increases rapidly, leading to the fractured recirculation flow above the surface. Until the flow influenced by the first pulse passes through the main bubble region, the flow structures above the corner enter a quasi-stable state, as shown in Fig. 15 (e) at t^* = 2.5. At the same time, the original induced separation bubble is locked upstream of the activation points. In the quasi-stable flow, under the impact of the entrained high momentum fluid, the main bubble is suppressed, but some fragmentary recirculation regions still exist near the corner. However, for a low PRF case, the reattachment point is only temporarily pushed downstream and fluctuates on the ramp surface close to the original reattachment point in the form of small fragmented vortices within the separation region. The original induced separation bubble is elongated, flattened, and moves downstream to coalesce with fragmented vortices. Notably, case C5 at L_p/L_0 = 0.50 and F^+ = 20, which has a higher PRF but the same excitation position, shares similar control authority with better performance. Correspondingly, Fig. 15 (f)-(j) show the "moving heat" evolution at different t^*. Compared to single pulse activation,

heat can be transported farther downstream of the activation point. However, it still dissipates in the shear flow very quickly. The process of destruction and reattachment of the shear layer remains in accordance with the evolution of the heated fluid transmitted downstream. At t^* = 0.5, with continuous activation, the heating region expands downstream, but the highest temperature core subsequently locks upstream of the corner, which is highly related to the applied PRF. Finally, the flow field tends to be quasi-stable, forming a heated and high-momentum boundary layer to suppress the main separation. It is noteworthy that the induced shock during the fast heating process may have little contribution to the induced vortices in the initial separation bubble. First, the perturbation to flow properties caused by the induced shock/compression waves is limited to a narrow region behind the shock front (see Fig. 6 compression wave region). Second, the induced shock/compression wave moves away from the discharge region and presents itself as a deformation of streamlines behind the shock front (see Fig. 13 (c1) IS). It decays rapidly and cannot access the recirculation area downstream. This implies that the flow field can be disrupted by the propagation of the induced shock, but the perturbation is transient and localized in the vicinity of the induced shock front. It provides little contribution to the changes in the flow field once the induced shock has exited the plasma region. The persistent effects are caused by the momentum entrainment into the separation region resulting from the residual heat region.

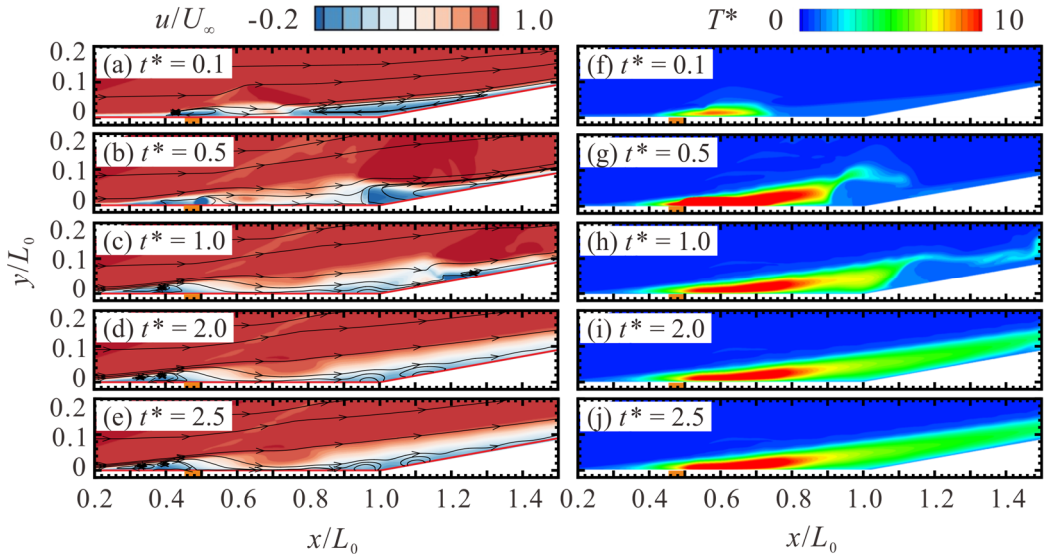

Fig. 15 Contours of instantaneous normalized streamwise velocity u/U_∞ (left column) with streamlines superimposed and nondimensional temperature T^* (right column) at t^* = (a)(f) 0.1; (b)(g) 0.5; (c)(h) 1.0 (d)(i) 2.0; and (e)(j) 2.5 of case C5 at L_p/L_0 = 0.50, F^+ = 10, and V = 50 kV.

For cases where the excitation position is far upstream of the main separation region, the control effects are limited. Initially, the entrained high momentum fluid enters the boundary layer before the main separation bubble. Then, it has a weak impact on the separation region and eventually dissipates in the shear layer. In this scenario, the heat dissipates in the boundary layer, and high momentum fluid is scarcely transferred into the separated region, resulting in a weak impact on the main separation bubble. Even so, the surface pressure around the reattachment point on the ramp still decreases significantly. By increasing the PRF, the suppression effect can be enhanced.

Compared to case C5, the actuators in case C6, which are installed downstream of the original separation point, may function more effectively on the separation suppression. In case C6 at F^+ = 10, the strong entrained momentum moves toward the bubble, as shown in Fig. 16 (b). The high momentum fluid impacts the reversed flow and totally breaks the original separated shear layer. The suppression of the main bubble is more effective than in case C5. There is almost no recirculation region above the ramp surface. More high momentum fluid is brought into the separation region to withstand the adverse pressure gradient. Note that, because of the coaction of both the adverse pressure gradient and heating effects, the induced separation bubble is larger than those of other cases.

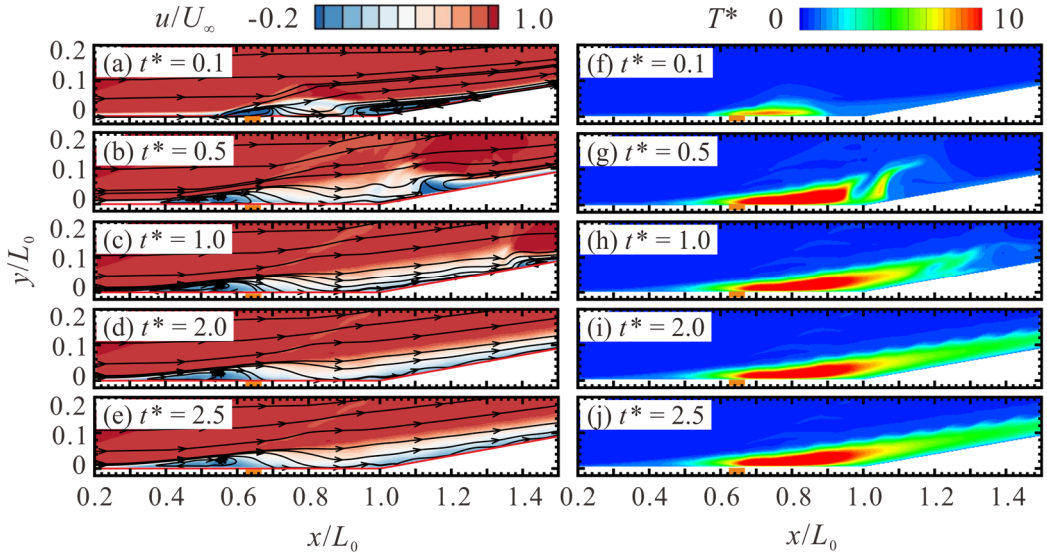

Fig. 16 Contours of instantaneous normalized streamwise velocity u/U_∞ (left column) with streamlines superimposed and nondimensional temperature T^* (right column) at t^* = (a)(f) 0.1; (b)(g) 0.5; (c)(h) 1.0 (d)(i) 2.0; and (e)(j) 2.5 of case C6 at L_p/L_0 = 0.67, F^+ = 10, and V = 50 kV.

The results in the periodic control suggest that increasing the PRF is an effective way to suppress the separation region. In summary, sufficient momentum exchange in the separation

region caused by the induced vortex is the major control mechanism. The presence of induced vortices is discernible upstream of the heated region, as observed by Aljohani et al.[53] in their investigation of surface heating elements within the boundary layer. They found that the strong wall heating may lead to a separated flow before the element is reached for supersonic flows, unlike subsonic flows in which the flow is more susceptible to separation behind the heating element. The strength and region of induced separation vortices increase with escalating voltage and PRF, resulting in enhanced momentum exchange that effectively impedes the primary separation near the corner. It is worth noting that the intensified induced separation vortices do not appear to impose significant detrimental effects on the flow characteristics, including the aerodynamic properties expounded extensively in the subsequent section. The excitation location is a dominant parameter that depends on the specific flow system and its local fluid characteristics. The results suggest that residual heat induces the initial vorticities and plays a dominant role in controlling separated flow. Moreover, supersonic flow exhibits a more resilient characteristic to thermal impact, and the shear layer breakup procedure is more complex. A more appropriate excitation near the separation point significantly increases control effectiveness.

4.5. Impact on the aerodynamic force

The aerodynamic response is a critical factor in flow control. The current study explores the possibility of adjusting an air vehicle's flight trajectory by utilizing the lift force generated from NSDBD as well as the potential for drag reduction on a specific geometry. Similar previous work was conducted by Gnemmi et al.[54], where an arc plasma discharge was employed to steer a supersonic projectile. Correale et at.[55] measured integral effects of the NSDBD plasma actuator on lift and drag over an airfoil. They found that under the stall conditions the lift increases up to 20% accompanied by drag reduction up to 3 times. In this section, surface pressure and skin friction are used to analyze the lift force and drag. And the Richardson number *Ri*, which is the ratio of the Grashof number *Gr* to the square of the Reynolds number *Re*, is used to determine if forced or free convection may be neglected for this system. *Ri* is estimated in the order of 10^{-5}, much smaller than 1, which means the free convection caused by buoyant force can be ignored in this case.

Fig. 17 shows the time-averaged skin friction coefficient for case C5 (50 kV, at $L_p/L_0 = 0.5$) in the quasi-stable state with different F^+. A sharp valley, seen in Fig. 17 (a) near the activation location, is caused by the heat impulse originating from the fast heating of the pulsed discharge. The actuation drops the surface friction upstream of the heating region and subsequently results

in a rebound downstream of it, which is consistent with the process of initial separation and reattachment due to the induced vortex. In the case of low-frequency activation at $F^+ = 1$ (red line), inside the separation bubble, the downstream local minimum increases after control. It is indicated that the effects of the NSDBD diminish the accelerated process caused by the favorable pressure (pointing upstream) in the recirculation boundary layer. After control, at the local peak near the corner (see the enlarged view in Fig. 17 (b), two separations marked with hollow circles and triangles) become positive, indicating the emergence of secondary separation near the corner beneath the main separation (see Fig. 10 (d)), which indicates vortices near the corner. The repeated separation and reattachment on the wall implies that the unsteady flow fluctuates around the corner. The fluctuating positive peaks illustrate its evolution. Compared to a low-frequency activation, a higher F^+ (= 10 or 20) causes a more significant local decrease in C_f, corresponding to a stronger adverse velocity in the induced vortex boundary layer. Although there may be fluctuations around the inflection point, the surface friction remains positive after the actuation location due to the suppression of separation.

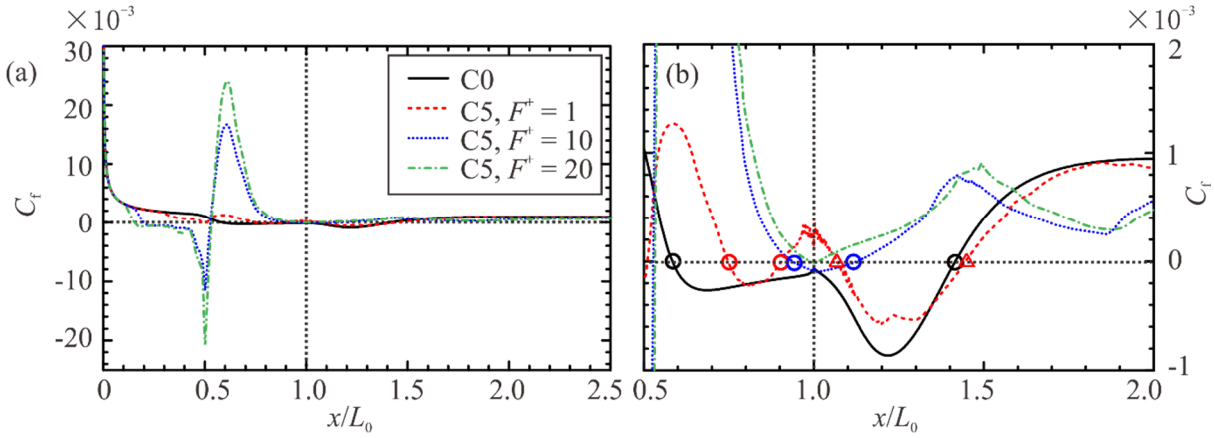

Fig. 17 (a) Distributions of the time-averaged skin friction coefficient for cases C5 (50 kV) at L_p/L_0 = 0.5 with different F^+ and (b) an enlarged view near the corner. Open circles and triangles: separation and reattachment points.

The time-averaged surface pressure coefficients in the quasi-stable state are presented in Fig. 18 for the cases of C2 (25 kV) and C5 (50 kV) at L_p/L_0 = 0.5 with different F^+. The surface pressure begins to increase upstream of the SP controlled by the free-interaction process[2]. The flow expansion caused by the fast heating process increases the local C_p, resulting in the SP moving downstream. The peak is followed by the plateau region, the value of which increases slightly after control. Notably, when the discharge energy is insufficient, the pressure peak cannot exceed the plateau value. If the upstream actuation is far from the SP (cases C1 and C4),

C_p will drop slightly before it rises again. Downstream of the inflection point, the pressure rises again near the reattachment point and reaches its peak value, which is mainly determined by oblique shock theory. In the cases with high-frequency control (F^+ = 10, 20, blue and green lines in Fig. 18), a significant pressure drop can be observed on the ramp surface occurring from the reattachment region, which causes a pressure drag reduction. It appears that the activation position is not a determining factor on the surface pressure drop around reattachment, as surface pressure can be reduced, provided that the plateau pressure value has been increased under the activation of NSDBD. The upstream pressure increase reduces the adverse pressure gradient, further reducing the bubble size and pressure on the ramp surface. Overall, the adverse pressure gradient on the ramp surface decreases. The pressure peak near the activation location indicates that the induced shock by the fast heating process impacts the surface and reflects on the upward side, further increasing the plateau value. The asymmetry of the peak illustrates its distortion under the interaction with the freestream.

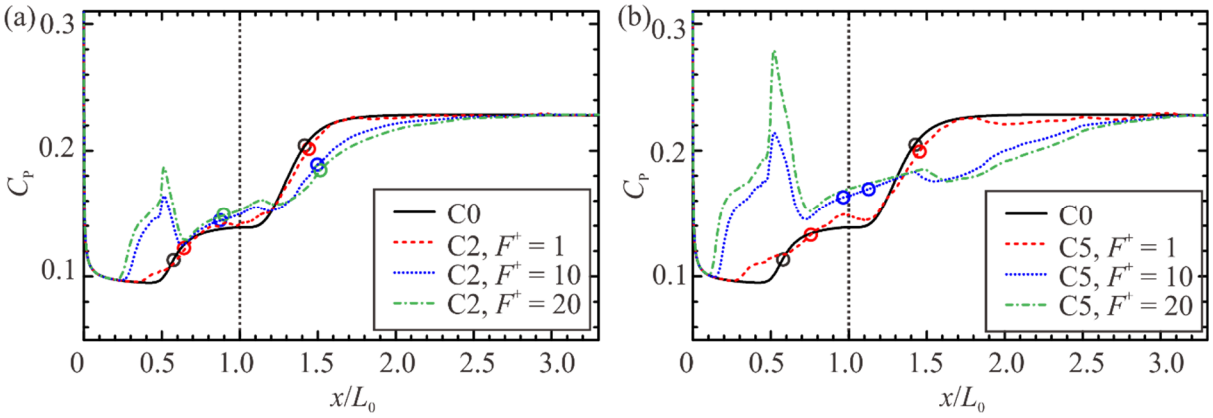

Fig. 18 Distributions of the time-averaged surface pressure coefficient at (a) C2 (25 kV) and (b) C5 (50 kV) at L_p/L_0 = 0.5 with different F^+. Open circles: separation and reattachment points.

The aerodynamic forces are calculated based on the integration of surface friction and pressure from x/L_0 = 0 to 3.3 at which the surface pressure has remained unchanged (see Fig. 18, mainly determined by the oblique shock theory). First, the time histories of the induced lift force and drag reduction with selected C4, C5 and C6 cases at F^+ = 10 are plotted in Fig. 19 (a). Apparently, the modification of surface flow structures will cause a change in surface aerodynamics. During the discharge process, there is a significant increase in pressure within the discharge volume, which subsequently relaxes. As a result, the lift force is initially generated in the negative y-axis direction, and then it decreases again at the next discharge before recovery. After several pulses, the lift change curve will be restored to the initial state

with oscillations that imply periodic lifting. The normal force produces a pitching moment, which can potentially be utilized to control the body's orientation and trajectory. The time histories of the force indicate that the flow field has undergone the process of establishment in a quasi-stable state. This can also be observed in drag evolution, and two processes are distinguished at approximately t^* = 1.5. On the other hand, the evolution of total drag consisting of pressure drag and friction drag appears to be more complex (Fig. 19 (b)). As the pressure drag represents the majority (96.8%) of the total drag, its distribution is similar to the total drag evolution. Generally, the pressure drag decreases significantly because the fluid entrainment decreases the adverse pressure gradient on the separation region. Subsequently, after the flow establishment, it slightly oscillates around a value under continuous activations. However, due to the high-speed flow entrainment, the skin friction drag increases, and the tendency is highly related to the flow structures depending on the activation locations. The skin friction enters the quasi-stable state earlier because it is affected by the entrained flow that occurs just downstream of the activation location, and the following flow structures have almost no influence on it. Note that the unequal values of the valleys (also seen in the peaks of the drag curve) are caused by the time resolution of the simulation data. However, due to the short integral time interval (1 μs), the time integral values (or time-averaged values) of lift and drag hardly change.

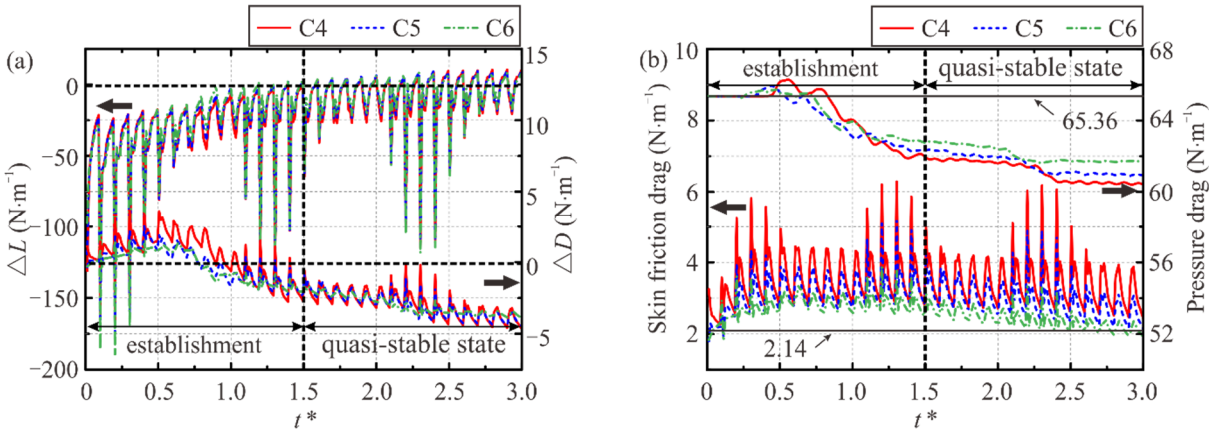

Fig. 19 (a) The lift and drag variations and (b) skin friction drag and pressure drag changes over time for a single pulse control of cases C4, C5, and C6.

To further investigate the time-averaged aerodynamics, the lift force and drag coefficient changes and reduction percentages of total drag, pressure drag and friction drag are summarized in Table 4. The data are time-averaged in the quasi-stable period from t^* = 1.5 to 3 (e.g., 15 activations at F^+ = 10). Overall, the case of L_p/L_0 = 0.67, F^+ = 20, and V = 50 kV shows the most drag reduction of 5.06%. As the frequency F^+ increases from 1 to 10, there is

a substantial increase in total drag reduction. However, as the frequency increases from 10 to 20, the drag reduction changes only insignificantly. This trend is similar to the suppression of the recirculation region. Notably, even when the excitation location is far from the SP, the drag is actually reduced, despite the lack of obvious bubble suppression. Interestingly, when the discharge energy is the same, the pressure drag reduction decreases significantly as the activated position moves downstream. This suggests that injecting momentum into the upstream boundary layer is more effective in enhancing the efficiency of pressure drag reduction. It is further indicated that momentum injection is more beneficial for withstanding the adverse pressure gradient. However, the activated position has the opposite effect on friction drag. This is because when the control position is farther from the separation point, more momentum is injected into the boundary layer due to the lower surface pressure. As the surface pressure gradually increases further downstream, more momentum is utilized to withstand the adverse pressure. Momentum injection in the boundary layer subsequently decreases, resulting in a decrease in the skin friction drag. Therefore, the total drag reduction effect is determined by the balance between the opposing effects of pressure drag and friction drag. In addition, because the separation bubble size is reduced in all controlled cases, the skin friction drag always increases.

Table 4 Time-averaged aerodynamic forces on the ramp surface.

Case	$\Delta C_L(\times 10^{-4})$	$\Delta C_D(\times 10^{-4})$	Total drag reduction(%)	Pressure drag reduction(%)	Friction drag reduction(%)
Baseline	−1844	272	67.50($N \cdot m^{-1}$)	65.36($N \cdot m^{-1}$)	2.14($N \cdot m^{-1}$)
C1, $F^+ = 1$	−1.91	−0.97	0.35	0.38	−0.50
C1, $F^+ = 10$	−4.71	−6.11	2.24	2.79	−14.36
C1, $F^+ = 20$	−10.71	−7.15	2.62	3.70	−30.23
C2, $F^+ = 1$	−2.42	−0.67	0.24	0.36	−3.48
C2, $F^+ = 10$	−3.99	−6.03	2.21	2.64	−11.08
C2, $F^+ = 20$	−9.94	−7.57	2.78	3.53	−20.33
C3, $F^+ = 1$	−3.18	−0.32	0.12	0.26	−4.21
C3, $F^+ = 10$	−3.92	−5.73	2.20	2.29	−3.64
C3, $F^+ = 20$	−9.96	−7.40	2.72	3.01	−6.17
C4, $F^+ = 1$	−5.16	−3.76	1.38	1.46	−0.96
C4, $F^+ = 10$	−37.89	−11.76	4.31	6.44	−60.61
C4, $F^+ = 20$	−80.66	−11.12	4.08	7.21	−91.63
C5, $F^+ = 1$	−6.54	−3.32	1.22	1.30	−1.14
C5, $F^+ = 10$	−31.82	−12.19	4.47	5.88	−38.46
C5, $F^+ = 20$	−69.56	−13.36	4.90	6.78	−52.36
C6, $F^+ = 1$	−5.33	−0.54	0.20	0.32	−3.59
C6, $F^+ = 10$	−31.00	−12.11	4.44	5.01	−13.08
C6, $F^+ = 20$	−66.56	−13.80	5.06	5.79	−17.14

Finally, the actuator efficiency can be defined as the mechanical power saved by drag reduction divided by the electric power provided to the actuator as shown using Eq.(9)[14, 56], shown as:

$$\eta = \frac{P_{saved}}{P_{input}} = \frac{\Delta D \cdot U_{\infty}}{E_{in} \cdot PRF} \tag{9}$$

where ΔD is the reduced drag on the surface after control. Relations between power saved and power cost are shown in Fig. 20. The efficiency of all cases is generally between 0.5% to 3%, as shown between the two black lines in Fig. 20. Overall, as the voltage and PRF are increased, the effectiveness of the plasma actuator in reducing drag diminishes. This implies that achieving further savings in mechanical energy necessitates using additional electrical energy. However, increasing the voltage remains more efficient than increasing the frequency. This finding aligns with the conclusion drawn regarding the control of the separation area size. It demonstrates that employing higher voltage and moderate frequency as a control strategy yields superior drag reduction effects and high energy efficiency, making it the optimal approach. Furthermore, the comparatively lower energy efficiency signifies ample potential for enhancement. The investigation of improving efficiency, including the incorporation of modulation frequency alongside the optimal PRF and the alteration of the electrode configuration, will be the subject of further research endeavors in the future.

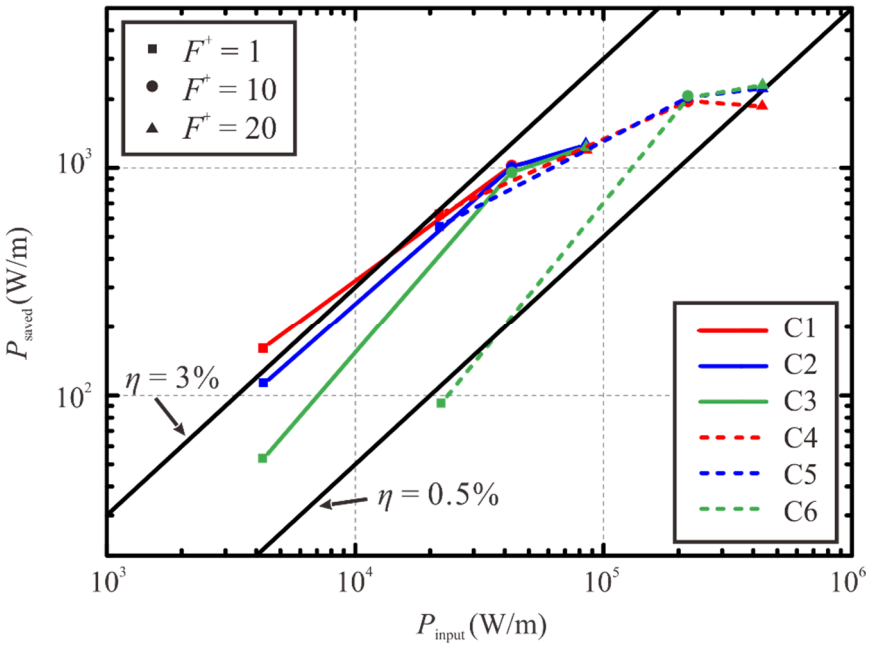

Fig. 20 Relations between power saved and power cost.

5. Conclusion

In this paper, flow control using an NSDBD on a laminar supersonic compression corner is investigated in detail to explore the probable control mechanism. The detailed results are summarized as follows:

(1) First, a one-zone inhomogeneous phenomenological plasma model is adopted to simulate the fast heating process of discharge. The vorticity transport equation is employed to analyze the formation mechanism of spanwise vorticity induced by plasma on a flat plate without freestream. The vorticities are primarily generated due to the pressure rise induced by the excitation and the consequent baroclinic torque caused by the misalignment between the pressure gradient and density gradient in the residual heat region.

(2) Second, the mechanism of separation suppression on a supersonic compression corner is discussed. Momentum migration is the primary mechanism behind the inhibition of separation flow. The induced vortex disrupts the initial flow field structure and entrains high-energy flow from the main flow into the boundary layer, promoting momentum mixing between the main flow and the separated flow. This increases the flow momentum inside the boundary layer and enhances its ability to resist the adverse pressure gradient. Under the interaction of the supersonic freestream and the plasma-induced shock/compression flow, the induced spanwise vortex is collectively generated by the convection, compressibility of the fluid element, and baroclinicity of the residual heat region. The induced vortex, in turn, facilitates momentum migration.

(3) For the investigation of control performance on the separated flow, the results suggest that improving the applied voltage is more effective than increasing the PRF if considering the energy consumption. It is possible to completely eliminate the flow separation on the supersonic compression corner. Further improving the F^+ from 10 to 20, the performance is better but limited. Moreover, applying a lower voltage but with a high activation frequency can also eliminate the bubble. This indicates that there is a critical F^+ that can eliminate the main separation and have a minimum side effect of the induced bubble. Moreover, excitation near the separation point achieves a higher effectiveness in suppressing the separation bubble for a supersonic compression corner.

(4) Based on the surface pressure and friction, the aerodynamics on the surface are studied. The normal force produces a pitching moment and may provide the body with an angle of attack, which can potentially be utilized to control the body's orientation and trajectory. On the other hand, total drag on the surface can be reduced by 5%. The pressure drag represents

the majority of the total drag and is reduced by 5% to 7% after control. However, the friction drag increases as the boundary layer becomes fuller after the control. The control performance on both the flow field and aerodynamic forces indicates that choosing the most appropriate position based on its local fluid characteristics will strongly increase the control effectiveness. In the current study, the case at $L_p/L_0 = 0.67$, $F^+ = 20$, and $V = 50$ kV shows the best performance in suppressing the separation region and drag reduction.

This study indicates that the NSDBD plasma actuator is a feasible and promising technique for separation control in a laminar supersonic flow. The results are expected to provide guidance for further experimental investigations and inspire new ideas for the application of this control technology. In the near future, we will conduct an experiment based on the findings of this study in our supersonic wind tunnel to further investigate the effectiveness of the NSDBD plasma actuator on controlling separation in supersonic flows.

Acknowledgments

The authors are grateful for the financial support provided by the Hong Kong Research Grants Council (no. 15206519, no. 15216621, no. 15217622 and no. 25203721) and the National Natural Science Foundation of China (no. 12102377).

References

[1] J. Hao, S. Cao, P. Guo, and C.-Y. Wen, "Response of Hypersonic Compression Corner Flow to Upstream Disturbances," *Journal of Fluid Mechanics,* vol. 964, 2023.
[2] J. Hao, S. Cao, C.-Y. Wen, and H. Olivier, "Occurrence of Global Instability in Hypersonic Compression Corner Flow," *Journal of Fluid Mechanics,* vol. 919, 2021, Art. no. 4.
[3] V. Theofilis, "On the Origins of Unsteadiness and Three-Dimensionality in a Laminar Separation Bubble," *Philosophical Transactions of the Royal Society of London. Series A: Mathematical, Physical and Engineering Sciences,* vol. 358, pp. 3229-3246, 2000, Art. no. 1777.
[4] V. Theofilis, "Global Linear Instability," *Annual Review of Fluid Mechanics,* vol. 43, no. 1, pp. 319-352, 2011.
[5] J. C. Robinet, "Bifurcations in Shock-Wave/Laminar-Boundary-Layer Interaction: Global Instability Approach," *Journal of Fluid Mechanics,* vol. 579, pp. 85-112, 2007.
[6] S. Cao, J. Hao, I. Klioutchnikov, H. Olivier, and C.-Y. Wen, "Unsteady Effects in a Hypersonic Compression Ramp Flow with Laminar Separation," *Journal of Fluid Mechanics,* vol. 912, 2021, Art. no. 3.
[7] J. G. Zheng, Y. D. Cui, and B. C. Khoo, "A Comparative Study of Alternating Current and Nanosecond Plasma Actuators in Flow Separation Control," *International Journal of Heat and Mass Transfer,* vol. 135, pp. 1097-1117, 2019.
[8] H. Yu and J. Zheng, "Investigation of Flow Separation Control over Airfoil Using Nanosecond Pulsed Plasma Actuator," *International Journal of Heat and Mass Transfer,* vol. 203, 2023.
[9] L. Shen, Z. N. Chen, and C.-Y. Wen, "Experimental Investigation of the Flow Structure over a Delta Wing Via Flow Visualization Methods," *J Vis Exp,* no. 134, Apr 23 2018.
[10] Z. Chen, L. Shen, and C.-Y. Wen, "Flow Control on a Bluff Body Using Dielectric Barrier Discharge Plasma Actuators," *AIAA Journal,* vol. 57, no. 7, pp. 2670-2674, 2019.
[11] Y. Liu, C. Kolbakir, H. Hu, and H. Hu, "A Comparison Study on the Thermal Effects in Dbd Plasma Actuation and Electrical Heating for Aircraft Icing Mitigation," *International Journal of Heat and Mass Transfer,* vol. 124, pp. 319-330, 2018.
[12] Y. Liu, C. Kolbakir, H. Hu, X. Meng, and H. Hu, "An Experimental Study on the Thermal Effects of Duty-Cycled Plasma Actuation Pertinent to Aircraft Icing Mitigation," *International Journal of Heat and Mass Transfer,* vol. 136, pp. 864-876, 2019.

[13] X. Deng and Z. Hou, "Thermal Characteristic and Spatial Morphology between Electrode and Phase Changing Ice During De-Icing Process of Dielectric Barrier Discharge and Critical Behavior of the Surface Charge Density," *International Journal of Heat and Mass Transfer,* vol. 190, 2022.
[14] Z. Chen and C.-Y. Wen, "Flow Control of a D-Shaped Bluff Body Using Different Dbd Plasma Actuators," *Journal of Fluids and Structures,* vol. 103, 2021, Art. no. 103292.
[15] M. Tang, Y. Wu, H. Wang, S. Guo, Z. Sun, and J. Sheng, "Characterization of Transverse Plasma Jet and Its Effects on Ramp Induced Separation," *Experimental Thermal and Fluid Science,* vol. 99, pp. 584-594, 2018.
[16] F. Liu, H. Yan, W. Zhan, and Y. Xue, "Effects of Steady and Pulsed Discharge Arcs on Shock Wave Control in Mach 2.5 Flow," *Aerospace Science and Technology,* vol. 93, 2019.
[17] Y. Wang, H. Zhang, Y. Wu, Y. Li, and Y. Zhu, "Supersonic Compressor Cascade Flow Control Using Plasma Actuation at Low Reynolds Number," *Physics of Fluids,* vol. 34, no. 2, 2022.
[18] A. Belinger, N. Naudé, J. P. Cambronne, and D. Caruana, "Plasma Synthetic Jet Actuator: Electrical and Optical Analysis of the Discharge," *Journal of Physics D: Applied Physics,* vol. 47, no. 34, 2014.
[19] C. A. Brown, "Scalability of the Localized Arc Filament Plasma Actuators," presented at the 29th AIAA Aeroacoustics Conference, Vancouver, British Columbia Canada, 5 - 7 May 2008, 2008.
[20] M. Nudnova, S. Kindusheva, and N. Aleksahdrov, "Rate of Plasma Thermalization of Pulsed Nanosecond Surface Dielectric Barrier Discharge," presented at the 8th AIAA Aerospace Sciences Meeting Including the New Horizons Forum and Aerospace Exposition, Orlando, Florida, 2010.
[21] J. G. Zheng, Y. D. Cui, J. Li, and B. C. Khoo, "A Note on Supersonic Flow Control with Nanosecond Plasma Actuator," *Physics of Fluids,* vol. 30, no. 4, 2018, Art. no. 040907.
[22] Z. Chen, C. C. Wong, and C.-Y. Wen, "Thermal Effects on the Performance of a Nanosecond Dielectric Barrier Discharge Plasma Actuator at Low Air Pressure," *Physics of Fluids,* vol. 35, no. 1, 2023, Art. no. 017110.
[23] M. Nishihara, K. Takashima, J. W. Rich, and I. V. Adamovich, "Mach 5 Bow Shock Control by a Nanosecond Pulse Surface Dielectric Barrier Discharge," *Physics of Fluids,* vol. 23, no. 6, 2011, Art. no. 066101.
[24] N. J. Bisek, J. Poggie, M. Nishihara, and I. Adamovich, "Hypersonic Flow over a Cylinder with a Nanosecond Pulse Electrical Discharge," *Journal of Thermophysics and Heat Transfer,* vol. 28, no. 1, pp. 18-26, 2014.
[25] K. Kinefuchi, A. Y. Starikovskiy, and R. B. Miles, "Control of Shock-Wave/Boundary-Layer Interaction Using Nanosecond-Pulsed Plasma Actuators," *Journal of Propulsion and Power,* vol. 34, no. 4, pp. 909-919, 2018.
[26] K. Kinefuchi, A. Y. Starikovskiy, and R. B. Miles, "Numerical Investigation of Nanosecond Pulsed Plasma Actuators for Control of Shock-Wave/Boundary-Layer Separation," *Physics of Fluids,* vol. 30, no. 10, 2018, Art. no. 106105.
[27] Z. Chen, L. Hao, and B. Zhang, "A Model for Nanosecond Pulsed Dielectric Barrier Discharge (Nsdbd) Actuator and Its Investigation on the Mechanisms of Separation Control over an Airfoil " *SCIENCE CHINA Technological Sciences,* vol. 56, pp. 1055–1065, 2013.
[28] K. Takashima, Z. Yin, and I. Adamovich, "Measurements and Kinetic Modeling Analysis of Energy Coupling in Nanosecond Pulse Dielectric Barrier Discharges," presented at the 43rd AIAA Plasmadynamics and Lasers Conference, 2012.
[29] K. Takashima, Y. Zuzeek, W. R. Lempert, and I. V. Adamovich, "Characterization of a Surface Dielectric Barrier Discharge Plasma Sustained by Repetitive Nanosecond Pulses," *Plasma Sources Science and Technology,* vol. 20, no. 5, 2011, Art. no. 055009.
[30] Manuel A. Rios, Maryia Nudnova, Svetlana Kindusheva, and Nikolay Aleksahdrov, "Fast Nonequilibrium Plasma Thermalization in N2-O2 Mixtures for Different Pulse Polarities and Its Application to Prevent Ice Formation," presented at the 49th AIAA Aerospace Sciences Meeting including the New Horizons Forum and Aerospace Exposition, Orlando, Florida, 2011.
[31] T. Unfer and J. P. Boeuf, "Modelling of a Nanosecond Surface Discharge Actuator," *Journal of Physics D: Applied Physics,* vol. 42, no. 19, 2009.
[32] C.-C. Wang and S. Roy, "Energy and Force Prediction for a Nanosecond Pulsed Dielectric Barrier Discharge Actuator," *Journal of Applied Physics,* vol. 111, no. 10, 2012.
[33] A. Montello, D. Burnette, M. Nishihara, W. R. Lempert, and I. V. Adamovich, "Dynamics of Rapid Localized Heating in Nanosecond Pulse Discharges for High Speed Flow Control," *Journal of Fluid Science and Technology,* vol. 8, no. 2, pp. 147-159, 2013.
[34] J. G. Zheng, Z. J. Zhao, J. Li, Y. D. Cui, and B. C. Khoo, "Numerical Simulation of Nanosecond Pulsed Dielectric Barrier Discharge Actuator in a Quiescent Flow," *Physics of Fluids,* vol. 26, no. 3, 2014, Art. no. 036102.
[35] J. Hao and C.-Y. Wen, "Effects of Vibrational Nonequilibrium on Hypersonic Shock-Wave/Laminar Boundary-Layer Interactions," *International Communications in Heat and Mass Transfer,* vol. 97, pp. 136-142, 2018.
[36] J. Hao, C.-Y. Wen, and J. Wang, "Numerical Investigation of Hypervelocity Shock-Wave/Boundary-Layer Interactions over a Double-Wedge Configuration," *International Journal of Heat and Mass Transfer,* vol. 138, pp. 277-292, 2019.
[37] J. Hao and C.-Y. Wen, "Hypersonic Flow over Spherically Blunted Double Cones," *Journal of Fluid Mechanics,* vol. 896, 2020, Art. no. 26.
[38] B. V. Leer, "Towards the Ultimate Conservative Difference Scheme," *Journal of computational physics,* vol. 32, pp. 101-136, 1979.
[39] M. J. Wright, G. V. Candler, and D. Bose, "Data-Parallel Line Relaxation Method for the Navier-Stokes Equations," *AIAA Journal,* vol. 36, no. 9, pp. 1603-1609, 1998.
[40] D. M. Peterson, "Simulations of Injection, Mixing, and Combustion in Supersonic Flow Using a Hybrid Rans/Les Approach," Doctor of Philosophy, The university of minnesota 2011.
[41] J. Hao, J. Fan, S. Cao, and C.-Y. Wen, "Three-Dimensionality of Hypersonic Laminar Flow over a Double Cone," *Journal of Fluid Mechanics,* vol. 935, 2022.
[42] Z. Chen, J. Hao, and C.-Y. Wen, "Control of Supersonic Compression Corner Flow Using a Plasma Actuator," *Physics of Fluids,* vol. 34, no. 7, 2022, Art. no. 073605.

[43] Z. J. Z. Y.D. Cui, Y. Bouremel, J. Li, J.G. Zheng, F.G. Hu and B.C. Khoo, "Studies on the Configurations of Nanosecond Dbd Pulse Plasma Actuators," presented at the 19th Australasian Fluid Mechanics Conference, Melbourne, Australia, 8-11 December 2014, 2014.
[44] Z. Zhao, J.-M. Li, J. Zheng, Y. D. Cui, and B. C. Khoo, "Study of Shock and Induced Flow Dynamics by Nanosecond Dielectric-Barrier-Discharge Plasma Actuators," *AIAA Journal,* vol. 53, no. 5, pp. 1336-1348, 2015.
[45] M. Kotsonis, S. Ghaemi, L. Veldhuis, and F. Scarano, "Measurement of the Body Force Field of Plasma Actuators," *Journal of Physics D: Applied Physics,* vol. 44, no. 4, 2011.
[46] J. Soni and S. Roy, "Design and Characterization of a Nano-Newton Resolution Thrust Stand," *Rev Sci Instrum,* vol. 84, no. 9, p. 095103, Sep 2013.
[47] N. A. Popov, "Investigation of the Mechanism for Rapid Heating of Nitrogen and Air in Gas Discharges," *Plasma Physics Reports,* vol. 27, pp. 886–896, 2001, Art. no. 10.
[48] M. Bleilebens and H. Olivier, "On the Influence of Elevated Surface Temperatures on Hypersonic Shock Wave/Boundary Layer Interaction at a Heated Ramp Model," *Shock Waves,* vol. 15, no. 5, pp. 301-312, 2006.
[49] K. Stewartson, F.R.S., and P. G. Williams, "Self-Induced Separation," *Proceedings of the Royal Society of London. A. Mathematical and Physical Sciences,* vol. 312, pp. 181-206, 1969.
[50] V. Y. Neiland, "Theory of Laminar Boundary Layer Separation in Supersonic Flow," *Fluid Dynanics,* vol. 4, pp. 53-57, 1969, Art. no. 4.
[51] O. Burggraf, "Asymptotic Theory of Separation and Reattachment of a Laminar Boundary Layer on a Compression Ramp," OHIO STATE UNIV RESEARCH FOUNDATION COLUMBUS1975.
[52] G. L. Korolev, J. S. B. Gajjar, and A. I. Ruban, "Once Again on the Supersonic Flow Separation near a Corner," *Journal of Fluid Mechanics,* vol. 463, pp. 173-199, 2002.
[53] A. F. Aljohani and J. S. B. Gajjar, "Transonic Flow over Localised Heating Elements in Boundary Layers," *Journal of Fluid Mechanics,* vol. 844, pp. 746-765, 2018.
[54] P. Gnemmi, R. Charon, J.-P. Dupéroux, and A. George, "Feasibility Study for Steering a Supersonic Projectile by a Plasma Actuator," *AIAA Journal,* vol. 46, no. 6, pp. 1308-1317, 2008.
[55] G. Correale, I.B. Popov, A.E. Rakitin, A.Yu. Starikovskii, S.J. Hulshoff, and L. L. M. Veldhuis, "Flow Separation Control on Airfoil with Pulsed Nanosecond Discharge Actuator," presented at the 49th AIAA Aerospace Sciences Meeting including the New Horizons Forum and Aerospace Exposition, Orlando, Florida, 4 - 7 January 2011, 2011.
[56] S. Roy, P. Zhao, A. DasGupta, and J. Soni, "Dielectric Barrier Discharge Actuator for Vehicle Drag Reduction at Highway Speeds," *AIP Advances,* vol. 6, no. 2, 2016.